STUDY OF PATCH ANTENNAS FOR STRAIN MEASUREMENT

By

UDAY SHANKAR TATA

Presented to the Faculty of the Graduate School of

The University of Texas at Arlington in Partial Fulfillment

of the Requirements

for the Degree of

MASTER OF SCIENCE IN ELECTRICAL ENGINEERING

THE UNIVERSITY OF TEXAS AT ARLINGTON

August 2008

ACKNOWLEDGEMENTS

I am grateful to my thesis advisor Prof. Huang for giving me the opportunity to be part of Advanced Sensor Technology Laboratory. It was a wonderful research experience to work with her. I thank Prof. Huang for devoting extra time and patience in guiding me during the research work at the lab. I am also thankful to her for providing financial assistance during the two years of my graduate study.

I thank Prof. Chiao for providing me knowledge on design and fabrication of antenna sensor. His ideas helped me in overcoming the experimental difficulties. I am thankful to Prof. Carter for serving in my thesis committee and providing me the access to the network analyzer and necessary test equipment for the experimental part of the thesis.

I would like to thank my father Kondala Rao, my mother Padmavathi, and my brother Ganesh for their love and support.

I thank Jiangqun Wang for training me on the network analyzer. I thank Thermpon Ativanichayaphong for his support during the mask design.

July 10, 2008

ABSTRACT

STUDY OF PATCH ANTENNAS FOR STRAIN MEASUREMENT

UDAY SHANKAR TATA, M.S.

The University of Texas at Arlington, 2008

Supervising Professor: Haiying Huang

Reliable strain measurement is important for damage detection of mechanical and civil structures. Existing wireless strain sensing technologies require a high operating voltage, bulky signal conditioning systems, and an external wireless module to transmit the sensor output. These limitations make the strain monitoring unreliable and expensive. An innovative method of measuring strain using a patch antenna is investigated in this thesis to overcome the limitations of existing strain sensing technologies. The patch antenna is made of a thin sheet of low-loss insulating material, called the dielectric substrate. The antenna pattern, i.e. a metallic patch, is printed on one side of the substrate. A ground plane is coated on the opposite side of the dielectric

substrate. The metallic patch and the ground plane form an electro-magnetic (EM) cavity. This EM cavity radiates at a resonant frequency that depends on the dimensions of the metallic patch. Strain changes the dimensions of patch antenna, resulting in a shift in the resonant frequency of patch antenna. First, single frequency and dual frequency antennas are designed using the transmission line model. The antenna design is then confirmed using an Electromagnetic (EM) simulation tool, Sonnet 11.5. Because the dual frequency antenna has two fundamental frequencies f_{010} and f_{010} corresponding to the antenna length and width respectively, it is sensitive to strains applied along the length and width direction. The single frequency antenna, however, has only one fundamental frequency f_{010}. Therefore, it is only sensitive to strains applied along the antenna length direction. In another word, strains applied along the antenna width direction do not have an effect on the frequency f_{010}. The effect of strain along the width and length direction of the dual frequency antenna and the width direction of the single frequency antenna on the antenna resonant frequency are simulated using Sonnet 11.5 and the strain sensitivity of the antenna is calculated for each case. The antennas are fabricated on a flexible Kapton substrate using conventional micromaching techniques. The effect of strain on the antenna resonant frequency is verified experimentally by bonding the antenna onto a cantilever beam and applying load at one end of the cantilever beam. The experimental and simulated results are in good agreement with each other.

TABLE OF CONTENTS

LIST OF ILLUSTRATIONS

LIST OF TABLES

CHAPTER 1

INTRODUCTION

The process of implementing sensors to check for damages in aerospace, civil, and mechanical structures is called Structural Heath Monitoring (SHM). SHM provides unique advantages such as better understanding and information about physical state of the structure on a continuous basis, potential elimination of catastrophic failure in operation, reduced downtimes and reduced preventive maintenance cost when compared to traditional fixed interval inspection cycles. The system can potentially reduce the life cycle costs and improve the safety of military aircrafts and next generation re-usable spacecrafts – a major area of interest for the DOD and NASA. Health monitoring systems are being considered for implementation on almost every new major air and spacecraft from the Lockheed Martin F-35 to the Boeing 7E7 to reusable space vehicles and have shown to be quite efficient under standard atmospheric conditions. The near term challenge is to develop a robust system, which is stable for long term and also capable of operating in severe environment such as high temperature, chemicals, electromagnetic interference etc. Future intelligent systems would not only be capable of detecting the damage in structure but would also employ smart healing technologies to heal that damage automatically especially if such damage is detected in outer space environment.

Timely damage detection is essential to prevent catastrophic structural failures. This can only be achieved when the operating parameters of the structures or the damage state of the load bearing structures are monitored continuously. Smart sensors that are capable of measuring either the damage state of load bearing structures directly or sensing the operating parameters such as temperature [1], pressure [2], strain [3], humidity [4], etc., is a very promising technology for SHM. Such sensors are capable of providing a rapid situational awareness regarding the damage state of a structure. They monitor either the physical state of the structure directly or measure critical operational parameters either on a continuous basis or by sending warning signals/alarm. These sensors have been broadly proposed for damage state assessment of re-usable space vehicles, international space station, military and commercial aircrafts, and civil infrastructure such as bridges, dams, offshore platforms and large buildings [5]. Smart sensor placed in strategic networks can be combined with wireless communication networks [7], distributed computing, software tools and intelligent decision tools to form an integrated system to provide a real time assessment of the structures under monitoring.

1.1 Importance of strain sensors for structural health monitoring

One of the principal requirements of a SHM system is load measurement capability. For civil structures, the main issues include sensing external loads, measuring the reaction of the structure to the external loads, and determining the internal state of health of the structure. External forces acting on a structure during its lifetime can include loads due to gravity, construction, traffic, earthquakes, weather, ocean waves and floods. The structure responds to these external loads by deforming and possibly degrading. The

sensing technologies used to assess the loads and their effects are strain sensing systems.

1.2 Proposed strain sensing system

The proposed strain sensing system consists of a rectangular patch antenna. Strain induces changes in the dimensions of patch antenna, resulting in a shift in the resonant frequency of patch antenna. A diagram of a typical patch antenna is shown in Figure 1.1. The patch antenna is made of a thin sheet of low-loss insulating material, called the dielectric substrate. The antenna pattern, i.e. a metallic patch, is printed on one side of the substrate. A ground plane is coated on the opposite side of the dielectric substrate. The metallic patch and the ground plane form an electro-magnetic (EM) cavity so that a resonance can be generated and the fringing field between the ground plane and the patch can efficiently radiate.

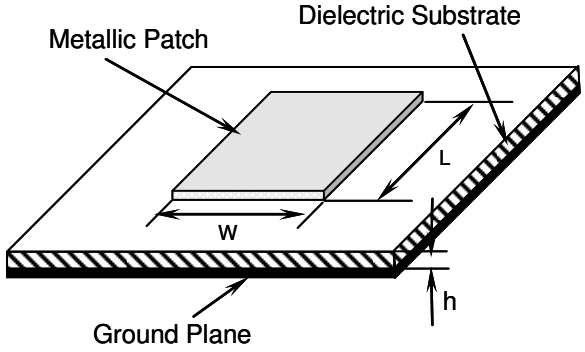

Figure 1.1: Patch antenna

The radiation behavior of the patch antenna can be described by Scattering Parameters, or S-parameters. S-parameters are a set of parameters describing the scattering and reflection of traveling waves when a network is inserted into a transmission line.

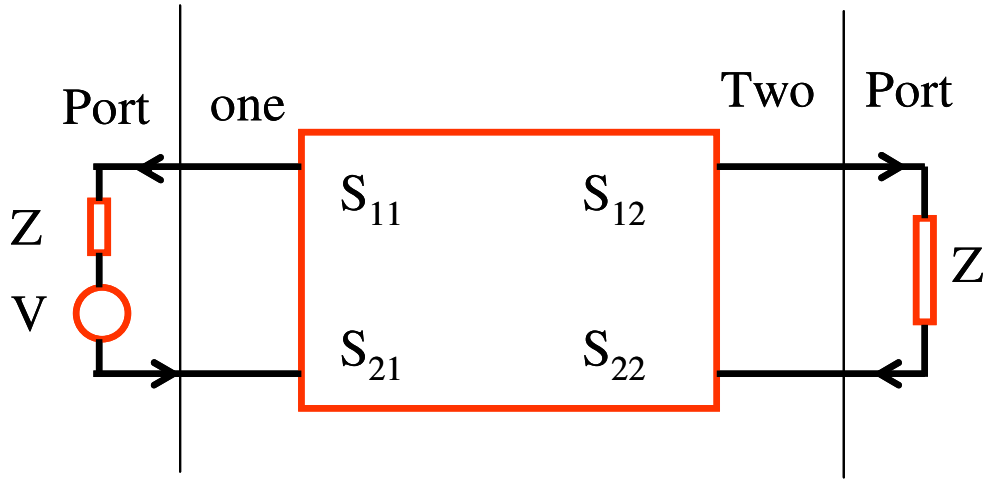

Figure 1.2 Two port network

Treating the patch antenna as a two-port microwave device, there are four s-parameters, denoted as S_{11} (input reflection coefficient of 50Ω terminated output), S_{21} (forward transmission coefficient of 50Ω terminated output), S_{12} (reverse transmission coefficient of 50Ω terminated input), and S_{22} (output reflection coefficient of 50Ω terminated input) as shown in Figure 1.2. Each parameter is typically characterized by a magnitude in decibels and a phase in radian. The S-parameters of the patch antenna can be measured using a network analyzer. A typical S_{11} curve of a patch antenna is shown in Figure 1.3(a). Return Loss is a parameter which indicates the amount of power that is "lost to the load" and does not return as a reflection. At the patch antenna resonant frequency, the return loss is the largest, resulting in a dip at the resonant frequency in the S_{11} curve. Figure 1.3 (b) shows the shifting of the resonant frequency towards its left side when a tensile strain is applied on the patch antenna.

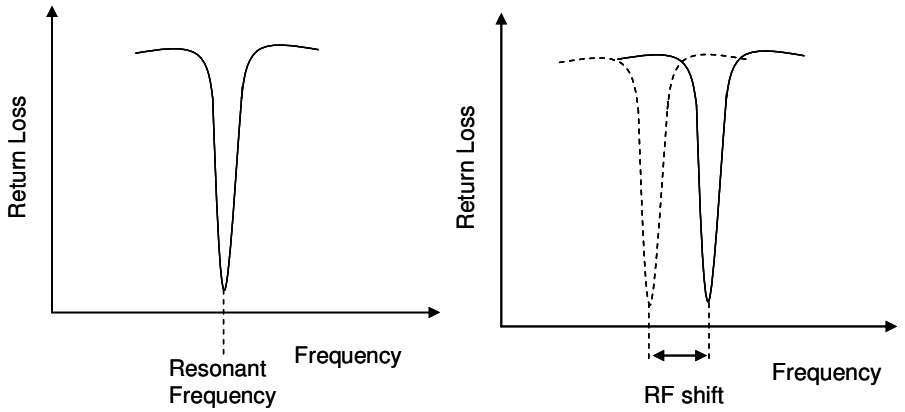

Figure 1.3: (a) Patch antenna frequency without strain (b) After strain.

1.3 Advantages of the antenna sensor over conventional strain gauges

To the best of our knowledge, this technique of using patch antenna itself as a strain sensor is the first attempt to employ patch antennas for strain measurement purpose. Compared to the conventional strain gauge, the proposed sensing technique offers many unique advantages, including:

- Resolution: The resolution of a patch antenna sensor is less than one microstrain while the resolution of strain gauges is limited to six microstrains.
- Lower operating voltages: The patch antenna sensor requires voltage as low as 0.7 V but operating voltages required in strain gauges are 10-20 V.
- No signal conditioning: The output of the patch antenna is frequency modulated where the output of conventional strain gauges is amplitude modulated. As a result, the output of the patch antenna sensor is less prone to ambient noises.

- No external wireless module: the resonant frequency of the antenna sensor can be interrogated wirelessly while the strain gauge requires an additional wireless module to transmit the signal.
- Multiplexing capabilities: The patch antenna can be multiplexed to form a wireless sensing network that can provide sensor coverage over a large area but multiplexing is very difficult in case of strain gauge sensors.

The differences between the antenna sensor and a conventional strain gauge are summarized in Table 1.1.

Table 1.1: Comparison of patch antenna sensor and strain gauge.

Features	**Strain gauge**	**Antenna sensor**
Resolution	6 μ ε	Less than 1μ ε
Source voltage	10-20 V	0.7 V
Signal modulation	Amplitude	Frequency
Signal conditioning	Yes	No
Wireless capability	Wired (needs external wireless system)	Yes
Multiplexing capability	No	Yes

1.4 Thesis indexing

Chapter 1 gives an introduction to SHM and an overview of the patch antenna strain sensor. Chapter 2 discusses microstrip patch antenna theory and the modeling of the antenna sensor using transmission line model and commercial software. The design of a dual frequency antenna and a single frequency antenna is also explained. In chapter 3, the operational principal of the patch antenna for strain measurement is discussed. The

relationship between strain and frequency is derived mathematically. Simulated frequency vs. RF characteristics of a dual frequency antenna when it is subjected to length and width direction elongation is explained. The sensitivity of f_{010} and f_{001} modal frequencies that correspond to the length and width direction elongation for the single and dual frequency antenna is elaborated. In chapter 4, the fabrication process of patch antenna is described. Different conventional integrated circuit fabrication techniques involved in the patch antenna design .Chapter 5 deals with different SMA connector configurations to feed the patch antenna when it is subjected to length or width direction elongation. The design of a cantilever beam and the experimental setup for applying strains to the antenna are described. The experimental results are compared with simulation results. Conclusions are given in chapter 6. Chapter 7 gives a brief description of future work.

CHAPTER 2

MICROSTRIP PATCH ANTENNA DESIGN

In this chapter, the fundamental working principle of a rectangular microstrip antenna, the linear transmission model, and the numerical simulation of antennas with different feeding techniques are discussed. In addition, the design of single and dual frequency patch antenna is discussed.

2.1 Introduction

Microstrip antenna patch elements are the most common form of printed antennas. They are popular because of their low profile, simple geometry, and low cost. A microstrip device in its simplest form is a layered structure with two parallel conductors separated by a thin dielectric substrate. The lower conductor acts as a ground plane. The device becomes a radiating microstrip antenna when one dimension of the upper conductor (the length L, the width w, or the substrate thickness h) is approximately equal to one half wavelengths.

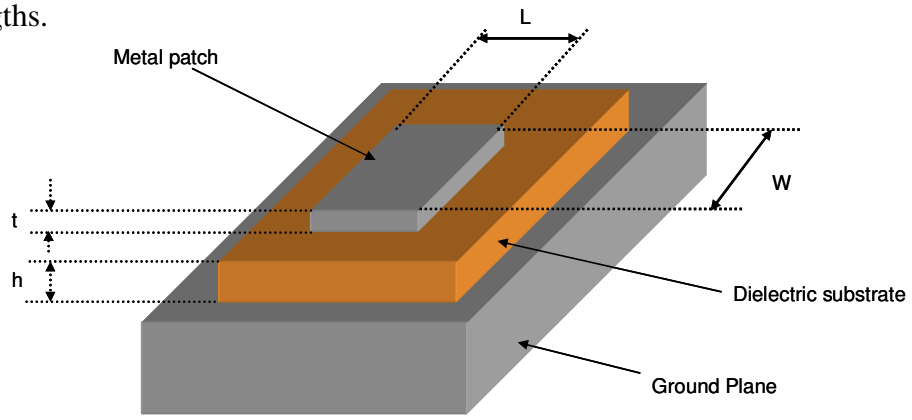

Figure 2.1: Diagram of a microstrip patch antenna.

2.2 Feeding techniques of patch antenna

Feeding of the patch antenna is required to send and receive RF signals to the patch antenna. There are numerous techniques to feed the microstrip patch antenna. The two most popular feeding methods are the microstripline feeding and coaxial probe feeding [8].

2.2.1 Microstripline feeding

In microstripline feeding, a microstripline is connected to the edge of the antenna. Usually, an inset is provided to match the input impedance, as shown in Figure 2.2. The microstripline fed patch antenna is easy to fabricate. As the substrate thickness increases, surface waves and spurious feed radiation increases which limits the bandwidth (typically 2%-5%).

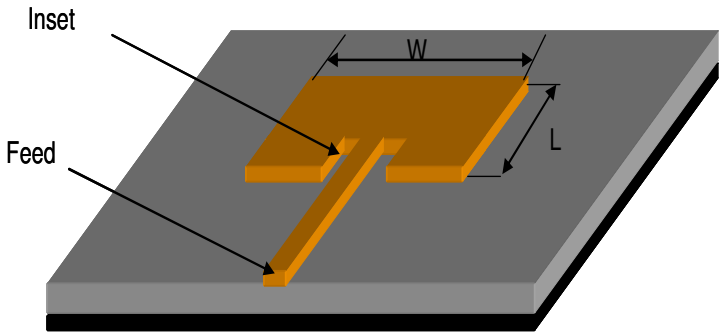

Figure 2.2: Microstripline feeding of patch antenna

2.2.2 Coaxial connector feeding

For coaxial connector feeding, a coaxial connector is used to the feed the RF power to the patch antenna, where the inner connector of the coax is attached to the metallic patch while the outer conductor is connected to the ground plane, as shown in Figure

2.3. The main advantage of this type of feeding scheme is that the feed can be placed at any desired location inside the patch in order to match with its input impedance. This feeding method is easy to fabricate and has low spurious radiation.

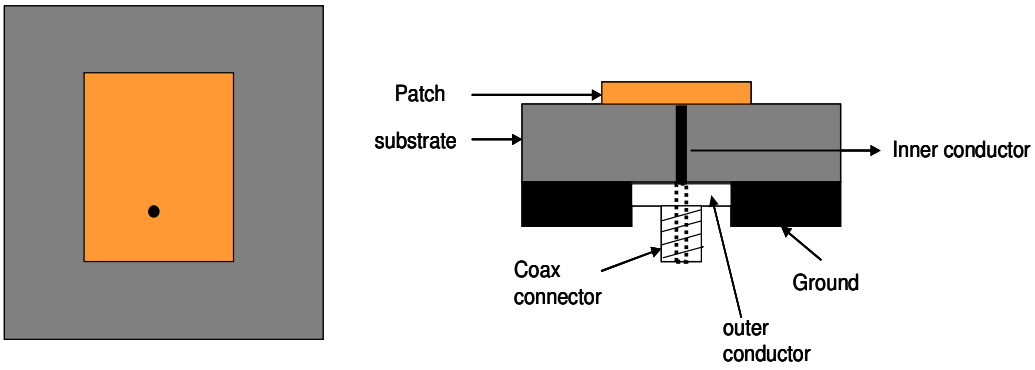

Figure 2.3: Coaxial feeding of patch antenna

2.3 Patch antenna modes of operation

Microstrip antennas resemble dielectric loaded cavities and they exhibit multiple resonances. As a result, the electric fields of different modes can co-exist inside the cavity. The resonant frequencies for the cavity is given by [8]

$$(f_r)_{mnp} = \frac{c}{2\pi\sqrt{\varepsilon_r}}\sqrt{\left(\frac{m\pi}{h}\right)^2 + \left(\frac{n\pi}{L}\right)^2 + \left(\frac{p\pi}{w}\right)^2}, \qquad (2.1)$$

where m, n, p represent, respectively, the number of half cycle field variations along the length, width and thickness directions. ε_r is the relative dielectric constant of the substrate, while c is the velocity of light in free space. h is the thickness of the substrate. L and w is the length and width of the patch antenna, respectively.

The radiation mode with the lowest order of resonant frequency is referred to as the dominant mode. To determine the dominant mode with the lowest resonance, we need

to examine the resonant frequencies of the cavity. Placing the resonant frequencies in ascending order determines the order of the modes of radiation. For all microstrip antennas, the substrate thickness h is much smaller than the dimensions of the upper conductor, i.e. h<<L and h<<w. If L>w>h, the mode with the lowest resonant frequency is the TM_{010} whose resonant frequency is given by

$$(f_r)_{010} = \frac{c}{2L\sqrt{\varepsilon_r}}. \tag{2.2}$$

If L>W>L/2>h, the mode with the lowest resonant frequency is the TM_{001} mode whose resonant frequency is given by

$$(f_r)_{001} = \frac{c}{2w\sqrt{\varepsilon_r}}. \tag{2.3}$$

The electric fields of the TM_{010} and TM_{001} mode are shown in Figure 2.4 (a) and Figure 2.4 (b) respectively. In TM_{010} mode the electric field varies in half wavelengths across the length direction of the antenna. Similarly in TM_{001} mode, the electric field varies across the width direction.

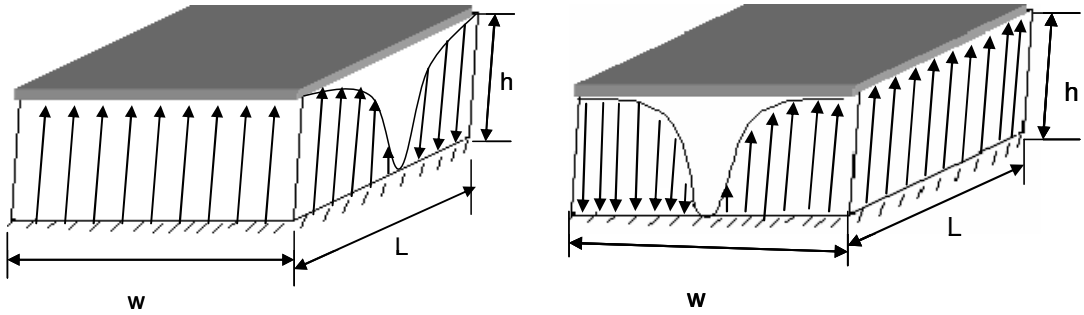

(a) (b)

Figure 2.4: (a) Field configurations forTM_{010} mode and (b) TM_{001} mode.

2.4 Transmission line model

The most popular and simple analytical model for a patch antenna is the transmission line model [8]. In transmission line model, the microstrip patch antenna is treated as a transmission line of length L, two slots of width w and a height of h, as shown in Figure 2.5. The patch antenna has two dielectric layers namely the air and the substrate. The electric field lines reside in both air and the substrate, as shown in Figure 2.6.

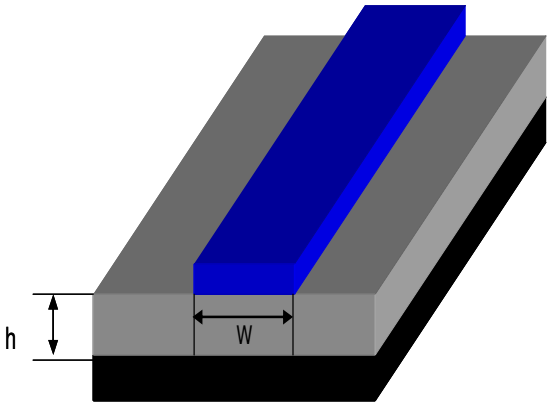

Figure 2.5: Microstrip line.

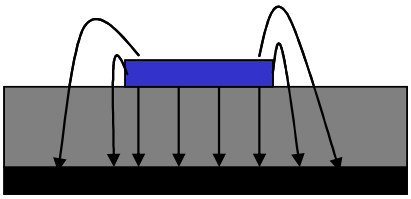

Figure 2.6: Electric field lines.

In order to consider fringing and wave propagation in the transmission line, an effective dielectric constant (ε_{re}) has to be found. The effective dielectric constant ε_{re} is slightly less than the dielectric constant of the substrate ε_r because the fringing fields around the patch is not confined to the dielectric but also spread into the surrounding air. The effective dielectric constant can be calculated from the relative dielectric constant of the substrate using Equation 2.4[8], i.e.

$$\varepsilon_{re} = \frac{\varepsilon_r + 1}{2} + \frac{\varepsilon_r - 1}{2\sqrt{(1 + 10h/w)}} \tag{2.4}$$

ε_{re} = Effective dielectric constant

ε_r = Dielectric constant of substrate

h = Height of dielectric substrate

w = Width of the patch

Consider a rectangular microstrip patch antenna of length L and width w resting on a substrate of height h, the coordinate axis of the patch antenna is selected such that the x direction is along the antenna length direction, the y direction is along the antenna width direction, and the z direction is along the antenna height direction. In order to operate in the fundamental TM_{010} mode, the length of the patch must be slightly less than $\lambda / 2$. The wavelength in the dielectric medium λ is equal to $\lambda_0 / \sqrt{\varepsilon_{re}}$, where λ_0 is the free space wavelength. The TM_{010} mode implies that the field varies one $\lambda / 2$ cycles along the antenna length direction and there is no variation along the width of the patch. The electric fields at the edges of the patch antenna can be decomposed into a normal component E_N and a tangential component E_T with respect to the ground plane, as shown in Figure 2.7.

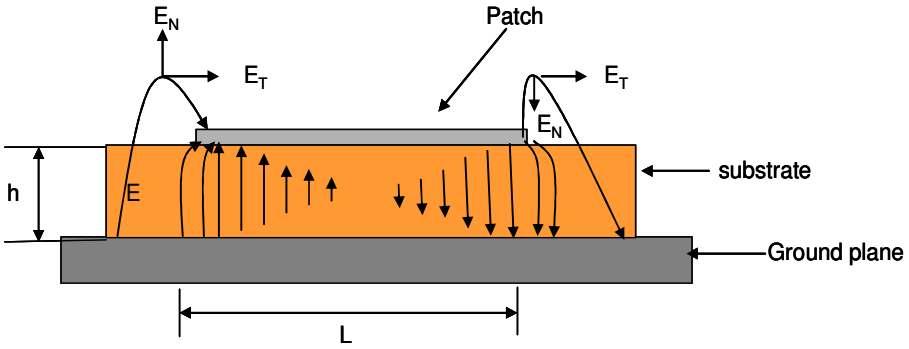

Figure 2.7: Side view of patch antenna fringing electric fields.

As shown in Figure 2.7, the normal components of the electric field E_N at the two edges are oriented at opposite directions and thus cancel each other. The tangential components are in phase, so that the resulting fields combine to give parallel radiated field normal to the surface of the structure [9]. The fringing fields along the width direction can be modeled as radiating slots. As a result, the patch antenna is electrically

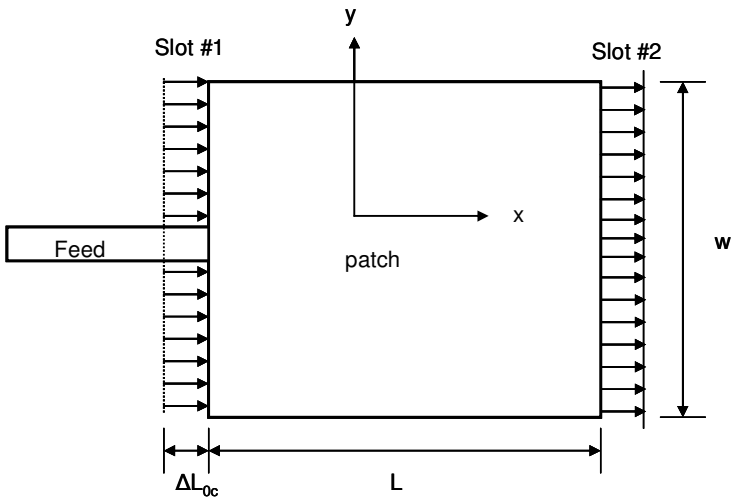

Figure 2.8: Top view showing tangential fringing electric fields that are responsible for radiation.

bigger than its physical dimensions, as shown in Figure 2.8. The dimensions of the patch along its length have now been extended at each end by a distance ΔL_{oc}, which is given empirically [8] as

$$\Delta L_{oc} = 0.412h \frac{(\varepsilon_{re} + 0.3)(w/h + 0.264)}{(\varepsilon_{re} - 0.258)(w/h + 0.813)} \tag{2.5}$$

The effective patch antenna length can be expressed as

$$L_{eff} = L + \Delta L_{oc} \tag{2.6}$$

The resonant frequency patch will be

$$f_r = \frac{c}{2\sqrt{\varepsilon_{re}}} \frac{1}{L + 2\Delta L_{oc}} \tag{2.7}$$

2.5 Design of the single frequency antenna

A single frequency patch antenna as shown in Figure 2.9(a) can be designed to operate at a desired resonant frequency for a chosen dielectric layer of thickness h and relative dielectric constant ε_r.The width of the patch antenna can be calculated as [8]

$$w = \frac{c}{2 f_r} \sqrt{\frac{2}{\varepsilon_r + 1}} \tag{2.8}$$

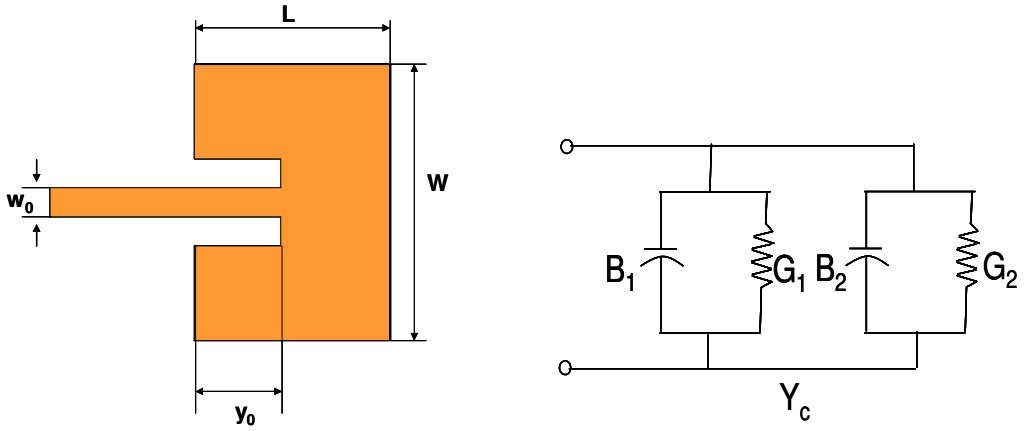

(a) (b)

Figure 2.9: (a) Single frequency antenna design and the (b) Equivalent electrical model.

The length of the patch is calculated as

$$L = \frac{c}{2f_r\sqrt{\varepsilon_{re}}} - 2\Delta L_{oc}, \tag{2.9}$$

where the effective dielectric constant ε_{re} is calculated using Equation 2.4 and the line extension ΔL_{oc} is calculated using Equation 2.5. The patch antenna can be electrically represented as shown in Figure 2.9(b). As the electric field radiates along width of the patch antenna, the width direction edges can be represented as two radiating slots of admittances Y_1 and Y_2 connected in parallel, where

$$Y_1 = G_1 + jB_1 \text{ and } Y_2 = G_2 + jB_2, \tag{2.10}$$

G_1, G_2 represent the conductance and B_1 and B_2 represent for the susceptance across the widths of the patch antenna. Since the two widths are identical, G_1=G_2 and B_1=B_2. G_1 is calculated as

$$G_1 = \frac{I_1}{120\pi^2}, \tag{2.11}$$

where I_1 is expressed as

$$I_1 = -2 + \cos(X) + XS_i(X) + \frac{\sin(X)}{X}, \tag{2.12}$$

$$X = k_0 w \text{ and } k_0 = \frac{2\pi}{\lambda_0}, \tag{2.13}$$

λ_0 is the wavelength in free space.

B_1 is expressed as

$$B_1 = \frac{w}{120\lambda_0}\left[1 - 0.636\ln(k_0 h)\right]. \tag{2.14}$$

If Y_{12} is the mutual admittance between the two radiating width direction slots then G_{12} is mutual conductance, it is expressed as

$$G_{12} = \frac{1}{120\pi^2}\int_0^{\pi}\left[\frac{\sin\left(\frac{k_o w}{2}\cos\theta\right)}{\cos\theta}\right]^2 J_0(k_0 L\sin\theta)\sin^3\theta d\theta\,, \qquad (2.15)$$

where J_0 is the zero order Bessel function.

In order to have an impedance matching for the patch antenna a feed inset y_0 is created. For a input impedance of 50 Ω the feed inset y_0 is calculated as

$$y_0 = \frac{L}{\pi}\cos^{-1}\left(\sqrt{100(G_1 + G_{12})}\right)\ . \qquad (2.16)$$

Using the above equations, a 20 GHz single frequency patch antenna on a 50 μm thick dielectric substrate with a relative dielectric constant of 3.4 is designed. The patch antenna is 5.056 mm in width and 4.037 mm in length. The feed inset is calculated to be 1.462 mm. The feed width, inset gap and feed length are chosen based on trial and error using Sonnet simulation tool.

2.6 Design of a dual frequency antenna

A dual frequency antenna is needed to measure strains along the length and with direction of the patch antenna. Antenna that has two dominating modes mainly TM_{010} and TM_{001} simultaneously is called dual frequency antenna. The resonant frequency corresponding to TM_{010} and TM_{001} are designated as f_{010} and f_{001} respectively.

A dual frequency patch antenna has been designed to operate at 15 GHz and 20.5 GHz on a 50 μm. polyimide substrate whose relative permittivity is 3.4. Initially the patch

antenna dimensions are calculated for 20.5 GHz resonant frequency using Equations 2.8 and 2.9. The length and width of the patch for 20.5 GHz resonant frequency are found to be 5.33 mm and 4 mm respectively. If the length and width dimensions are swapped and corresponding resonant frequency is calculated to be 15 GHz. As such, the TM_{010} mode frequency (15GHz) corresponds to the antenna length L and the TM_{001} mode frequency (20.5 GHz) corresponds to the antenna width w.

2.6.1 Procedure to determine the feeding point of dual frequency patch antenna

The two operation frequencies are mainly determined from the rectangular patch dimensions and the substrate permittivity. The feed position is selected such that the TM_{010} and TM_{001} modes are excited simultaneously. Figure 2.10 shows the feeding configuration of a rectangular dual frequency microstrip patch antenna.

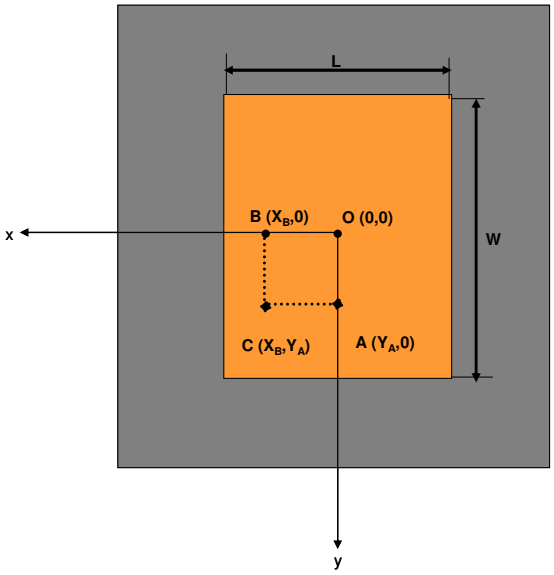

Figure 2.10: Feeding configuration of the dual frequency antenna.

When the antenna is fed at a point along the y axis, the TM_{010} mode of the patch antenna is excited only because it is dominant mode in length direction. When the

antenna is fed at a point along the x axis, the TM_{001} mode can be selectively excited, as it is the dominant mode in the width direction of the patch antenna. In order to match the 50 Ω impedance of the patch antenna, the feeding point A (0, Y_A) for the TM_{010} mode is calculated by equation 2.16 and the feeding point B (X_B, 0) for the TM_{001} mode can be calculated by replacing L value by w in equation 2.16 [10]. Both TM_{010} and TM_{001} modes are generated simultaneously by feeding the antenna at point C (X_B, Y_A).

2.7 Verification of antenna design

2.7.1 Simulation model of single frequency antenna using Sonnet

The antenna is simulated using an EM simulation tool, Sonnet 11.5. In the simulation editor, an 8mm × 10 mm × 6 mm metal box is created. The bottom surface of the metal box is selected as the ground plane for the patch antenna. The 50μm polyimide film with a relative dielectric constant of 3.4 is created as substrate material above the ground plane. The single frequency patch antenna of required dimensions is drawn on top of the dielectric substrate, as shown in Figure 2.11. The single frequency patch antenna dimensions are assigned as parameters so that they can be easily changed later for a particular strain condition. Initially the dimensions of the patch antenna are set to the values as calculated using transmission model equations for a 20 GHz frequency. A top view of the patch antenna is shown in Figure 2.12. The feed of the patch antenna is connected to the ground using an edge via. The parameters relating to feed such as feed width, feed length and the inset gap width on either sides of the feed are chosen by trial and error method so that there is maximum return loss at the resonant frequency. The maximum return loss indicates good impedance matching between the feed and the

patch antenna. The feed width is chosen to be 1mm, the length of the feed is 5.49 mm and the inset gap width is 1mm on either side of the feed.

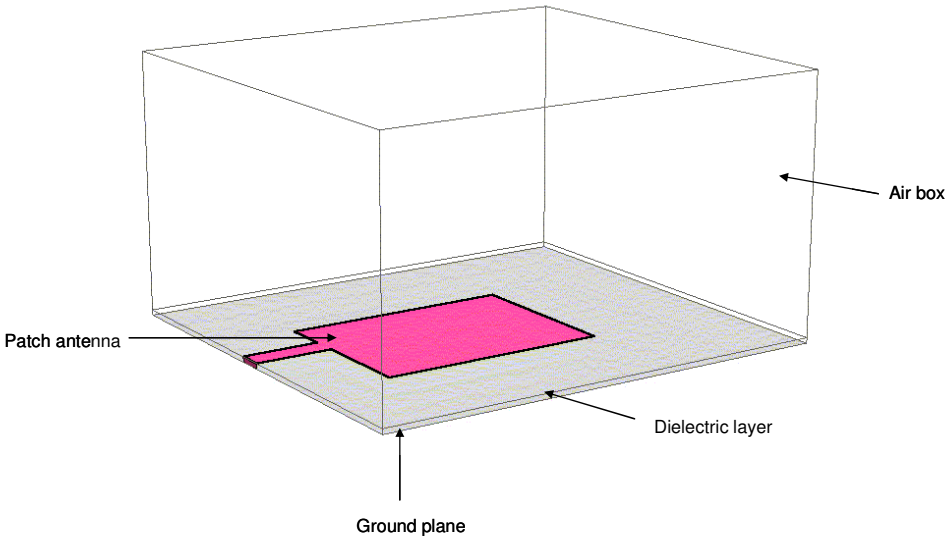

Figure 2.11: 3D simulation model of the patch antenna.

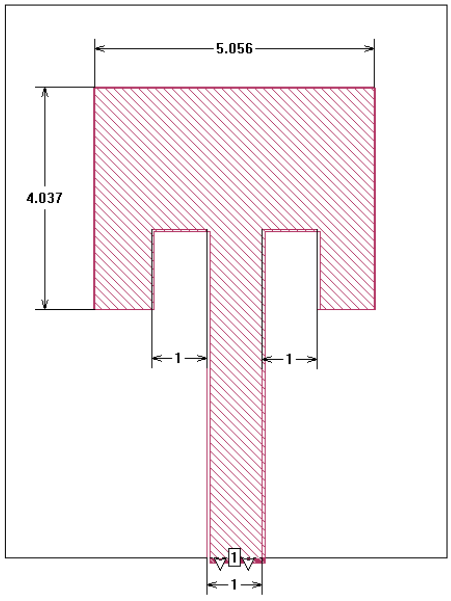

Figure 2.12: Single frequency patch antenna parameters in the simulation model.

A total of 2500 cells with each cell having a dimension of 0.004 mm × 0.0032 mm is used for the simulation. Figure 2.13 shows the Graphic User Interface (GUI) of the mesh settings. A linear sweep mode is used to sweep the frequency in steps of 0.01 GHz. The output data is exported to as excel file.

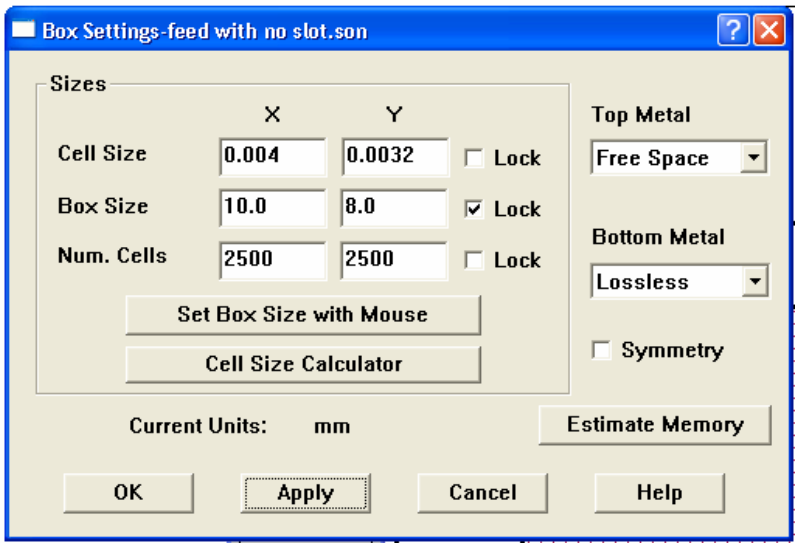

Figure 2.13: Mesh setting for the simulation model.

A similar procedure is followed for the simulation of dual frequency antenna. A narrow feed width can be designed to exactly the match the dual frequency impedance point C, but eventually it leads to improper electrical connection between SMA connector and the feed of the patch. As a result a wider feed width of 0.8 mm is designed. In addition, the antenna impedance was only matched for the TM_{001} mode because no inset is designed to match the impedance for the TM_{010} mode.

2.7.2 Simulation results of single and dual frequency antenna

The simulated resonant frequency of 20 GHz single frequency antenna is at 19.35 GHz. Figure 2.14 shows the simulated S_{11} curve for single frequency antenna indicating the

resonant frequency at 19.35GHz and return loss of -28 db. The dual frequency antenna with calculated dimensions is simulated and the simulated f_{010} is at 14.9 GHz and f_{001} frequency is at 19.55 GHz, which is compared to 15GHz and 20.5 GHz calculated frequencies respectively. The return loss at the 15 GHz is significantly less than the return loss at 20.5 GHz. This is because the TM_{010} mode is fed at the edge instead of at the impedance matching point. Figure 2.15 (a) shows the simulation model and (b) corresponding resonant frequencies of dual frequency patch antenna.

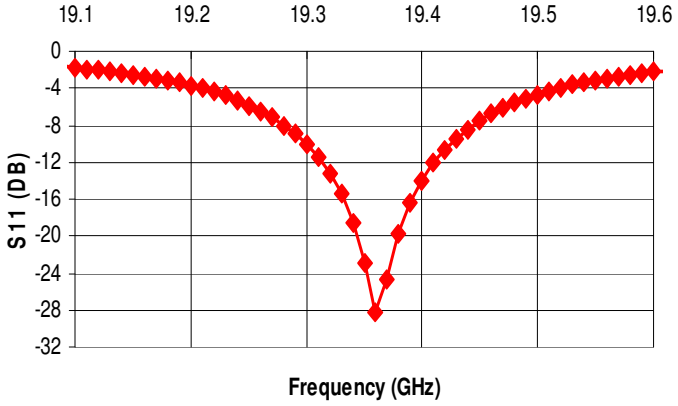

Figure 2.14: Simulation results of single frequency patch antenna.

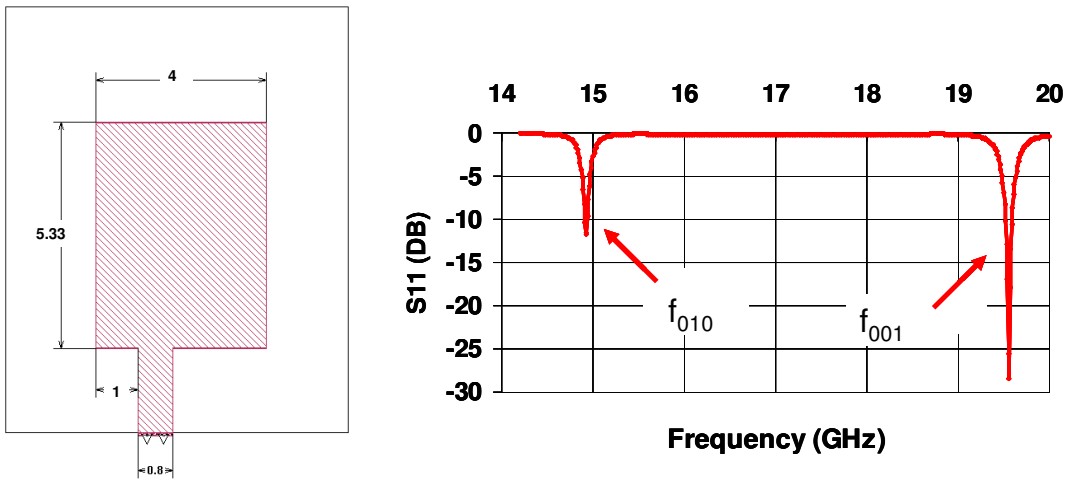

(a) (b)

Figure 2.15: (a) Designed dual frequency antenna (b) Simulation results.

CHAPTER 3

SIMULATION OF PATCH ANTENNA FOR STRAIN SENSING

In this chapter, the relation between the applied strain and the relative change of the antenna frequency is derived mathematically. The effect of strain on the antenna R.F along both the length and width direction is simulated using Sonnet.

3.1 Analysis of the relationship between strain and antenna resonant frequency using transmission line model

Based on the transmission line model [11], the resonant frequency of a rectangular patch antenna is calculated as

$$f_r = \frac{c}{2\sqrt{\varepsilon_{re}}} \frac{1}{L + 2\Delta L_{oc}} \tag{3.1}$$

c: velocity of light

ε_{re}: effective dielectric constant of the microstrip antenna

L: length of antenna patch

ΔL_{oc}: line extension.

The effective dielectric constant ε_{re} is given in Equation 2.4 and the line extension ΔL_{oc} is given in Equation 2.5. Assuming the antenna is subjected to a tensile strain ε_L along the length direction, the patch width and the substrate thickness will change due to Poisson's effect, i.e.

$$w = (1 - \upsilon_p \varepsilon_L) w_0 \text{, and } h = (1 - \upsilon_s \varepsilon_L) h_0 \ . \tag{3.2}$$

If the Poisson's ratios of the metallic patch and the substrate material, υ_p and $\upsilon_{s,}$ are the same, the ratio w/h remains to be a constant as the tensile strain ε_L changes, which means that ε_{re} in Equation 2.4 is independent of ε_L and ΔL_{oc} in Equation 2.5 is proportional to the substrate thickness h. Therefore, the resonant frequency in Equation 3.1 can be expressed as

$$f_r = \frac{c}{2\sqrt{\varepsilon_{re}}} \frac{1}{L + 2\Delta L_{oc}} = \frac{C_1}{L + C_2 h} . \tag{3.3}$$

$$C_1 = \frac{c}{2\sqrt{\varepsilon_{re}}} \quad C_2 = 0.812 \frac{(\varepsilon_{re} + 0.3)(w/h + 0.264)}{(\varepsilon_{re} - 0.258)(w/h + 0.813)} \ . \tag{3.4}$$

The strain-induced elongation, therefore, will shift the antenna resonant frequency. At an unloaded state, the antenna frequency f_{r0} is calculated from the antenna length L_0 and substrate thickness h_0,

$$f_{ro} = \frac{C_1}{L_0 + C_2 h_o} \ . \tag{3.5}$$

Under a strain ε_L, the antenna frequency shifts to

$$f_r(\varepsilon_L) = \frac{C_1}{L_o(1 + \varepsilon_L) + C_2 h_o (1 - \upsilon \varepsilon_L)} \ . \tag{3.6}$$

Combining Equation 3.5 and 3.6, we can establish the relationship between the strain ε_L and the frequency shift Δf,

$$\varepsilon_L = -\frac{L_o + \upsilon_s C_2 h_o}{L_o + C_2 h_o}\frac{\Delta f}{f_r} = C\frac{\Delta f}{f_r}, \tag{3.7}$$

$$\frac{\Delta f}{f_r} = K\varepsilon_L \ , \tag{3.8}$$

where $\Delta f = f_r - f_{r0}$. Analyzing the constant K indicates that the sensitivity of frequency shift to the applied strain is strongly governed by the dielectric constant of the substrate material.

3.2 Numerical simulation of strain-frequency relationship for a patch antenna

3.2.1 Length direction elongation of the dual frequency patch antenna

In order to simulate the effect of the length direction strain on the antenna frequency the dimensions of the patch antenna under strain are calculated as

$$L = (1+\varepsilon_L)L_0 \ , \ w = (1-\upsilon_p\varepsilon_L)w_0 \text{ , and } \ h = (1-\upsilon_s\varepsilon_L)h_0, \tag{3.9}$$

where L_0 is the antenna length, w_0 is the antenna width, and h_0 is the height of the substrate before the strain is applied. ε_L is the strain applied along the antenna length direction. υ_p and υ_s, are the Poisson's ratios of the metallic patch and the substrate material, respectively. The typical values are L_0=5.33 mm, w_0=4 mm, h_0=50 μm, υ_p=0.3 and υ_s=0.3. Table 3.1 shows the dimensions of the patch antenna when it is subjected to different strain levels.

Table 3.1: Patch antenna dimensions at different strains in length direction

Strain (%)	w (mm)	L (mm)	h (μm)
0	4.00	5.33	50
0.2	3.9976	5.3407	49.97
0.4	3.9952	5.3513	49.94
0.6	3.9928	5.3620	49.91

In the simulation model, the excitation frequency is swept from 14.2 GHz to 15.6 GHz in steps of 0.01 GHz. This particular band is chosen because the change in the length affects the f_{010} frequency only, which is 15 GHz. Figure 3.1 shows the simulated S_{11} curve of the patch antenna when it is subjected to strains ranging from 0% to 0.6%. We can observe a consistent shift in the resonant frequency of the patch antenna. As the applied tensile strain increases, the length of the patch increases and thus the S_{11} curve shifts parallel to its left side.

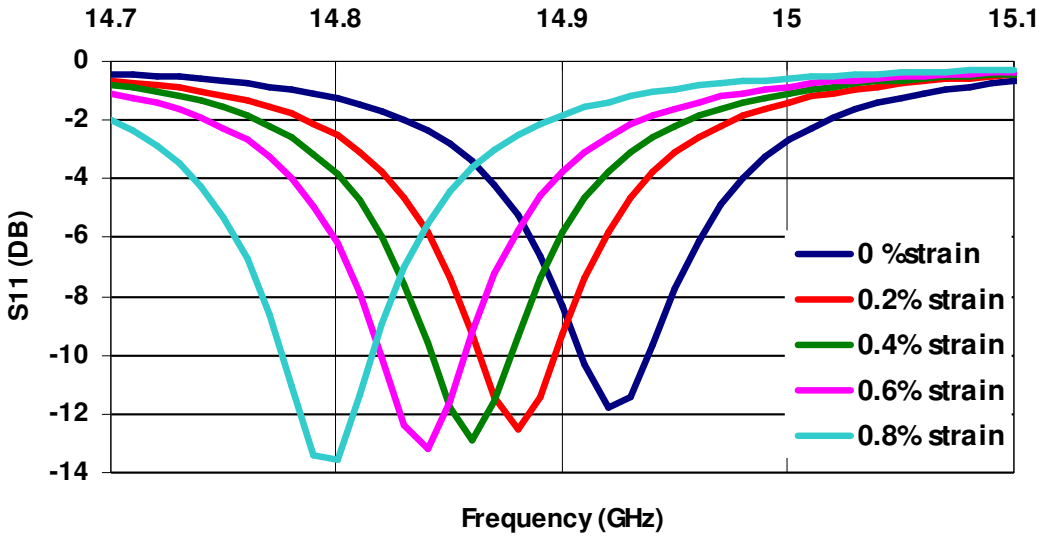

Figure 3.1: Simulated frequency response of the antenna under strains along the length direction.

The percentage of change in the antenna frequency is calculated for each strained condition as

$$\text{Relative change in frequency } (\%) = \left(\frac{f_r(\varepsilon_L) - f_{r0}}{f_{r0}} \right) \times 100 \quad , \tag{3.10}$$

where f_r (ε_L) is the antenna resonant frequency at a particular strained condition and f_{r0} is the antenna resonant frequency when no strain is applied. Figure 3.2 shows the relationship between the relative change in frequency and the applied strain for the length direction elongation of the dual frequency patch antenna. The slope of the graph gives the strain sensitivity of the sensor. In this case, the strain sensitivity of the antenna sensor is 0.983, which corresponds to 14.69 kHz/microstrain.

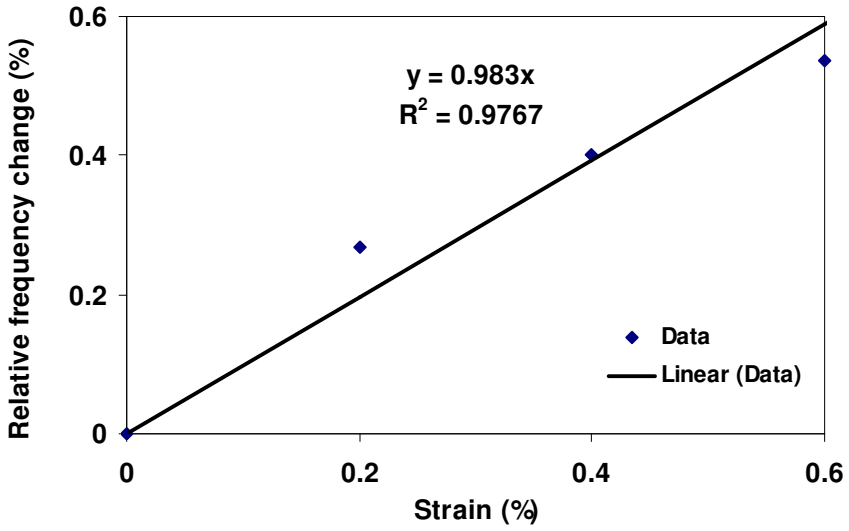

Figure 3.2: Simulated relationship between the percentage of change in antenna frequency and the applied strain along the length direction of a dual frequency patch antenna

3.2.2 Width direction elongation of the dual frequency patch antenna

Similarly, the dimensions of the patch antenna under strains applied along the width direction of the antenna are calculated as

$$w = (1+\varepsilon_w)w_0 \ , \ L = (1-\upsilon_p\varepsilon_w)L_0 \text{ and } \ h = (1-\upsilon_s\varepsilon_w)h_0 \ , \qquad (3.11)$$

where ε_w is the strain applied long the width direction of the antenna.

Table 3.2: Patch antenna dimensions at different strains in the width direction

Strain (%)	w (mm)	L (mm)	h (μm)
0	4.00	5.33	50
0.2	4.008	5.3268	49.97
0.4	4.016	5.3236	49.94
0.6	4.024	5.3204	49.91

The calculated dimensions of the patch antenna under a width direction strain ranging From 0% to 0.6% is shown in Table 3.2. In order to find out the effect of width direction strains on the resonant frequency of patch antenna, the frequency is swept from 18.6 GHz to 20.0 GHz in steps of 0.01 GHz. This particular band is chosen because the change in the antenna length only affects the f_{001} frequency, which is 20 GHz.

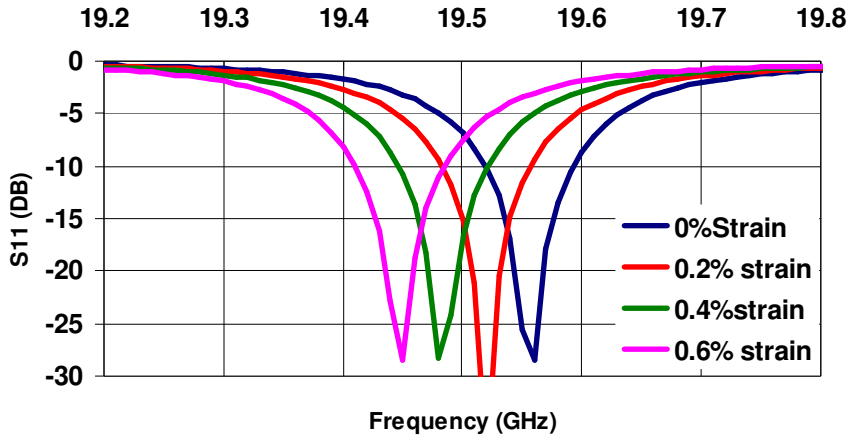

Figure 3.3: Simulated frequency response of the antenna under strains along the width direction.

Simulated S_{11} curve of the antenna under 0 -0.6% strains are shown in Figure 3.3. We can observe a consistent shift in the resonant frequency of the patch antenna. As the applied tensile strain increases, the width of the patch increases and the S_{11} curve shifts parallel to its left side. Similarly, the percentage of change in the antenna resonant frequency is calculated for each strained condition using Equation 3.11. Figure 3.4 shows the relationship between the relative change in frequency and the applied strain for width direction elongation of the dual frequency patch antenna. The slope of the graph gives the strain sensitivity of the sensor. It is estimated that the strain sensitivity of the sensor is 0.9725, corresponding to 19 kHz/microstrain.

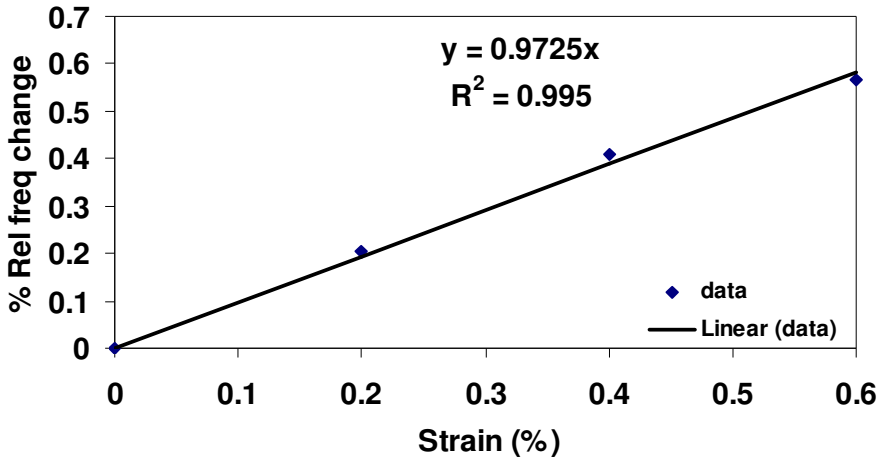

Figure 3.4: Simulated relationship between the percentage of change in antenna frequency and the applied strain along the width direction of a dual frequency

For a dual frequency patch antenna, the elongation of patch antenna along the width or length direction changes the corresponding modal frequency. This means that f_{010} is sensitive to the length direction elongation and f_{001} is sensitive to the width direction only. So in order to prove that f_{001} frequency is not sensitive to length direction elongation and f_{010} frequency is not sensitive to width direction elongation, one of the ways is to consider a single frequency patch antenna which has TM_{010} mode only and no other mode generated in the width direction. When the single frequency antenna is elongated along width direction, the f_{010} frequency should remain constant. The Figure 3.5 shows the simulated results for width direction elongation of single frequency antenna. It is evident that the f_{001} frequency is not sensitive to the width direction elongation.

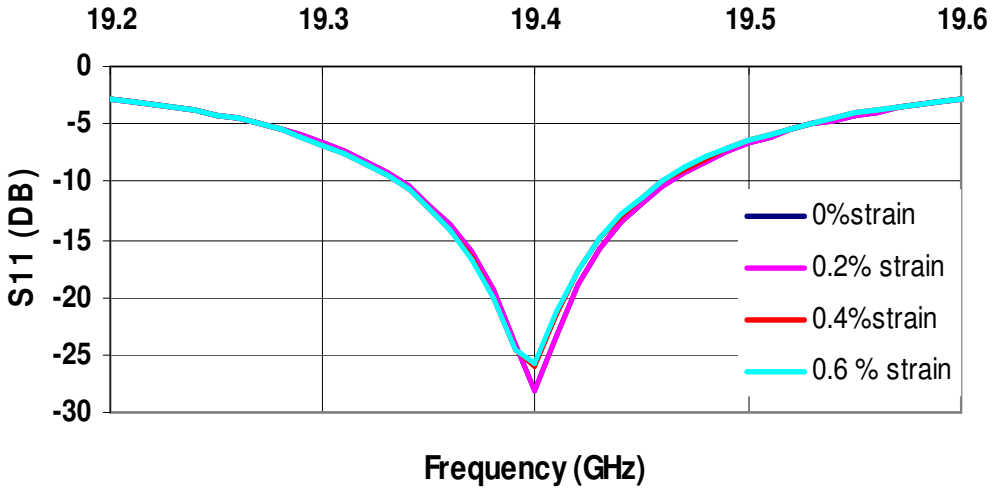

Figure 3.5: Simulated frequency response of the single frequency antenna under strains applied along the antenna in width direction

3.3 Summary of simulation results

Based on the simulation results, we can conclude that the f_{010} frequency i.e. (14.95 GHz) of the dual frequency antenna is sensitive to strain along the length direction and the sensitivity is found to be 0.983 (14.69 kHz/microstrain). On the other hand, the f_{001} frequency (19.55 GHz) of the dual frequency antenna is sensitive to the strains along the width direction and the sensitivity is found to be 0.9725 (19 kHz/microstrain). Single frequency antenna subjected to the width direction strain is also simulated and it was found that its f_{010} frequency is insensitive to strain applied along the width direction.

CHAPTER 4

SENSOR FABRICATION

The antenna sensors are fabricated using micromachining technology. Micromachining is mainly classified into two processes, namely bulk and surface micromachining. Bulk micromachining is a subtractive process where material is etched from the substrate to fabricate required device while surface micromachining is an additive process. Thin films of different materials are deposited and etched accordingly to obtain the desired structure. Micromachining technology has series of fabrication process such as lithography, photoresist developing, deposition, and etching. In this chapter patch antenna pattern design and fabrication is discussed.

4.1 Introduction to micromachining

This section will discuss a general overview of the micromachining processes, such as photolithography, metal deposition using thermal evaporation, and liftoff process. Following the introduction, the fabrication processes of the patch antenna is discussed. The flow diagram of the antenna fabrication process is shown in Figure 4.1

4.1.1 Mask design

A mask is a glass or polymer sheet with dark and clear patterns. The light passes through the clear patterns to exactly transfer the required pattern onto the substrate. There are two types of masks such as clear field and dark field mask. In the clear field

mask, the final pattern which is needed will be opaque and the rest of the area is transparent. In the dark field mask, the required final pattern is transparent and the rest

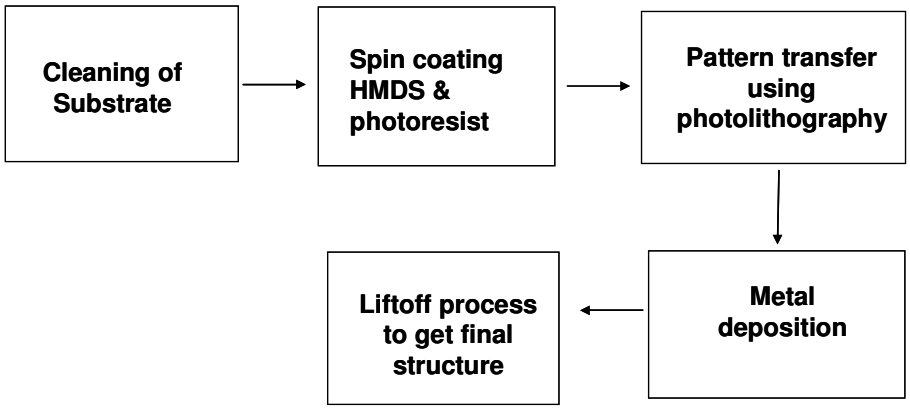

Figure 4.1: Fabrication process flow diagram.

of the area is opaque. After finalizing the antenna dimensions, a mask is designed to transfer the patch antenna pattern onto a required substrate. L-Edit pro 9.0 software is used to design the mask with exact patch antenna dimensions.

Figure 4.2 shows the fabricated mask on a myler (polyester) film by photoploting technology.

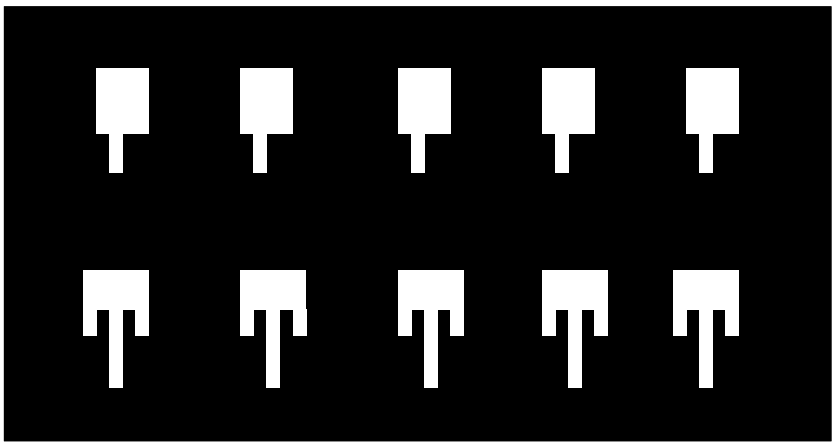

Figure 4.2: Mask with both single frequency and dual frequency antenna patterns.

4.1.2 Thermal evaporation

In thermal evaporation, a refractory metal plate is used to evaporate desired metal which is to be deposited onto the substrate. The refractory metal plate is called a boat and the mostly used metal for the boat is tungsten. The thermal evaporator consists of a vacuum chamber. Vacuum is created using rough and high vacuum pump. Vacuum is required in order to create a mean free path for the metal atoms to move towards the substrate and get deposited. The pressure inside the chamber is maintained in the order of 10^{-6} Torr. The current through the boat is increased to make it red hot and which in turn melts the metal pallets in it. The typical current values are 60-200 Amps. The typical deposition rate is 3-5 A^{o}/ sec. The deposition rate can be increased by increasing the current. Figure 4.3 shows the thermal evaporator equipment setup. [12]

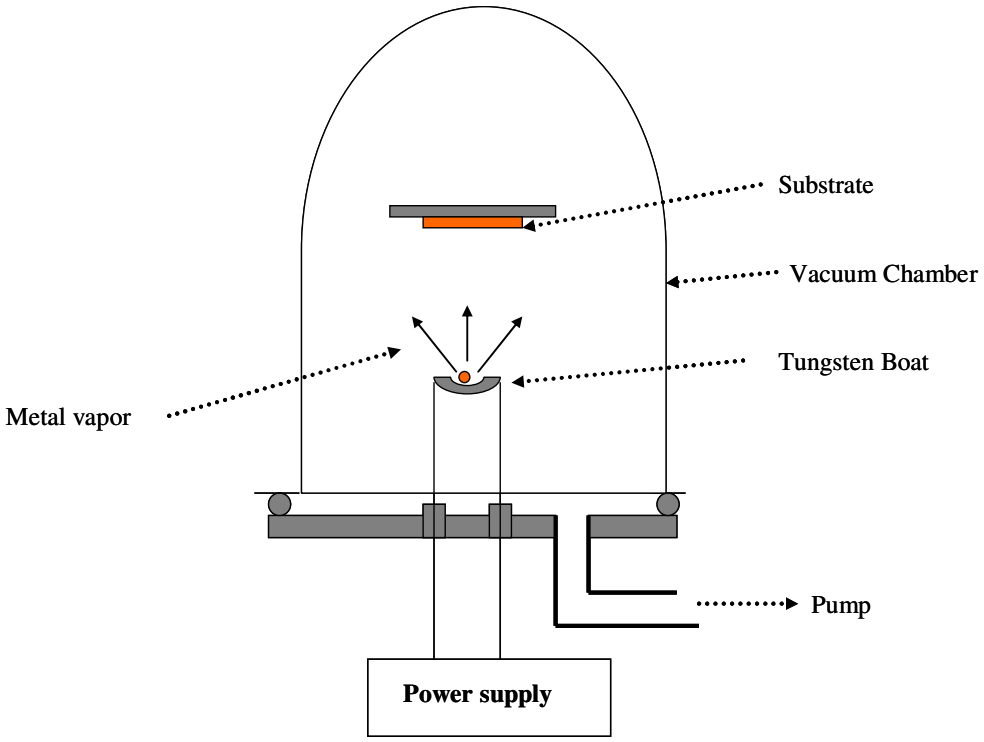

Figure 4.3: Thermal evaporator.

4.1.3 Photolithography

Photolithography has series of process such as spin coating of photoresist, soft baking, UV exposing and developing.

4.1.3.1. Spin coating of photoresist

Photoresist is applied to the substrate in a liquid form with the help of a dropper. The substrate is held on a vacuum chuck. The vacuum check is perforated and the air is sucked through these holes so that vacuum is created between the substrate and the chuck. As a result the substrate is held firmly to chuck. The chuck is spun typically at a high speed of 1000 rpm to 5000 rpm for 30 to 60 sec to produce thin uniform layer with thickness 2.5 um to 0.5um respectively. The thickness of the film depends on the speed of the chuck and the viscosity of the resist. Generally photoresist has bad adhesion to the substrate so the substrate is coated with a thin film of hexamethyldisiliazane (HMDS) prior to application of photoresist

4.1.3.2 Soft baking

The purpose of soft baking is to prevent the photoresist from sticking to the mask by removing the solvent from the photoresist and thus improve its adhesion to the substrate. The typical baking temperatures are from 60^0 to 100^0 C for a period of 5 to 10 min. the exact specifications will be provided by manufacturer which has to be followed closely. For S1813 photoresist the specified soft baking temperature is 100^0c

4.1.3.3 Photoresist exposure and developing

The photoresist was exposed through the mask using a high intensity ultraviolet light. There are two types of photoresist; one of them is positive photoresist and the other is

negative photoresist. In the case of positive photoresist, the area which is exposed to light gets polymerized and washes away after developing and the unexposed area stays on the substrate. In the case of negative photoresist the area that is exposed to UV light gets polymerized and stays after developing. The choice of the photoresist depends on the kind of mask and design of the structure required to be fabricated. Figure 4.4 show the comparison between negative and positive photo resist. For positive photoresist S1813, the developer solution used is MF319.

4.2 Liftoff process

Any thin film material above the photoresist layer can be removed when the entire structure is dipped into photoresist solvent or stripper. The most common solvent used is acetone. For the liftoff to happen, the metal should be very much thinner than the thickness of the photoresist. Typically, the photoresist thickness should be at least twice the metal thickness. if this is not the case, unwanted metal will stick to the edges of the desired structure and prevent the forming of sharp edges.

4.3. Fabrication procedure for patch antenna

The patch antenna fabrication has series of procedures and recipes. The fabrication flow diagram is shown in Figure 4.5

1. **Cleaning:** Initially a 50 μm polyimide film (Kapton HN) is cut into 4" × 4" square strips and is rinsed with acetone to clean the surface The Kapton strip can be sonicated in the acetone for a few minutes if the Kapton surface has grease. After cleaning, the Kapton strip is blow-dried using dry nitrogen.

2. **Spin coating:** The Kapton strips are placed directly on the vacuum chuck of a spin coater using a tweezer. A layer of hexamethyldisiliazane (HMDS) is first spin coated on the Kapton strips at a speed of 2000 rpm for 30 seconds. S1813 positive photoresist is then coated with the same speed and time recipe. According to the manufacturer specifications of S1813 photoresist, this particular recipe gives a film with a thickness of 1.5 μm.
3. **Soft baking:** After spin coating, the Kapton strips are soft baking on a hotplate at a constant temperature of 100^0C for one minute.
4. **Pattern transfer:** The mask fabricated on Mylar sheet is taped on a glass plate using a transparent adhesive tape, which serves as a glass mask that can be easily mounted onto the KARLSUSS^{TM} mask aligner. The Kapton strips are exposed for 15 seconds with a UV light power of 350W and an intensity of 25mW/cm^2 to transfer the patch antenna pattern from the mask to the photoresist. The mask used is dark field, where the patch antenna pattern is transparent and the rest of the mask is opaque, as shown in Figure 4.2. When the UV light passes through the mask, the photoresist is polymerized with the antenna pattern.
5. **Photoresist develop:** The Kapton strips are submerged in MF319 developer for 30 seconds to remove the polymerized photoresist so that the Kapton surface with the antenna pattern is exposed. The developed Kapton strips are rinsed with DI water and blow-dried using dry nitrogen.

6. **Thermal deposition:** 1μm thickness copper film is deposited onto the developed Kapton strips using thermal evaporation. During deposition, the pressure of the vacuum chamber is maintained at 5×10^{-6} Torr and the current used to heat the tungsten boat is 60 amps.
7. **Liftoff:** The Kapton strips are left in pure acetone for 3 hours to etch the developed photoresist which in turn lifts the metal on it. After lift off, only the desired antenna pattern remains on the Kapton. The unwanted metal sticking to the edges of the antenna can be removed by sonication for 2 minutes.

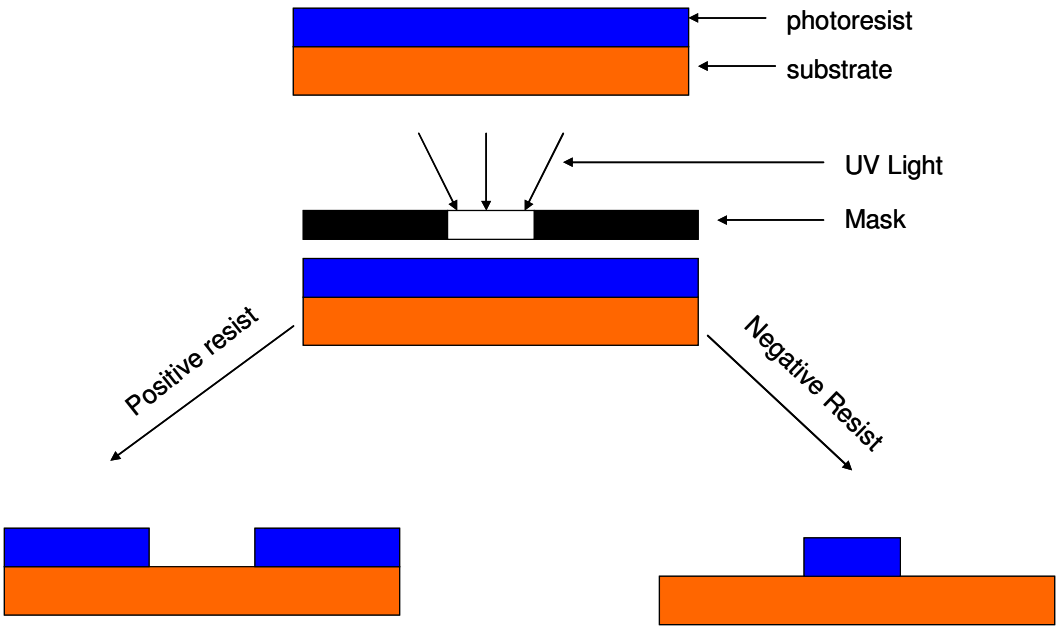

Figure 4.4: Comparison of negative and positive photoresist.

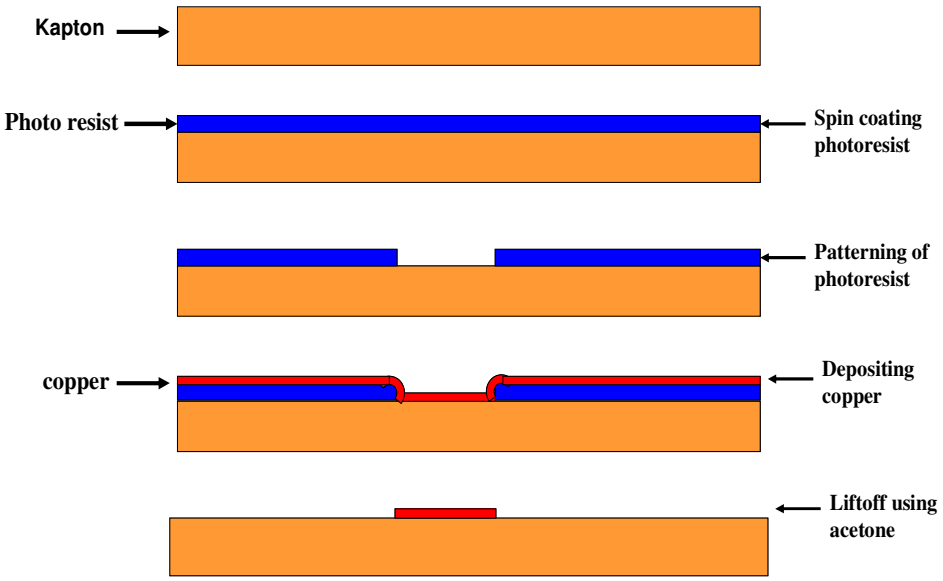

Figure 4.5: Fabrication steps of the patch antenna.

The fabricated dual and single frequency patch antenna with the above mentioned process is shown in Figure 4.6. The yellow material is the Kapton substrate and the metallic patch is made of copper.

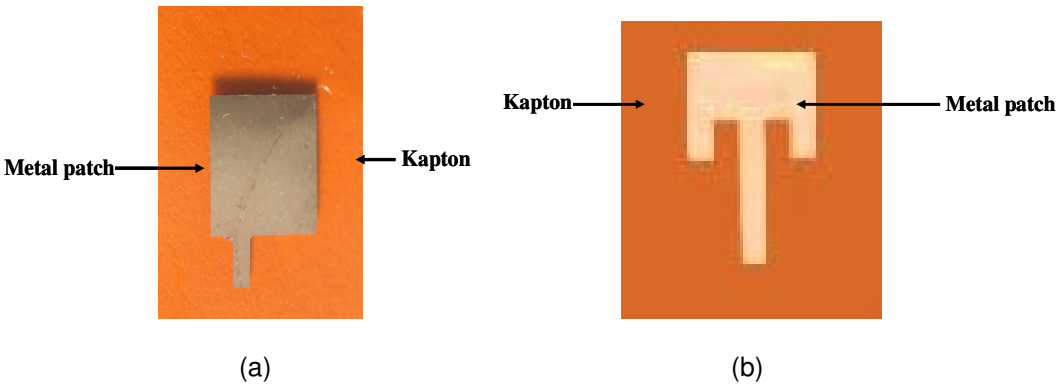

Figure 4.6: Fabricated (a) dual frequency and (b) single frequency patch antenna.

CHAPTER 5

EXPERIMENTAL SETUP AND RESULTS

In order to test the antenna patch for strain measurement, a special cantilever loading system is designed to apply strain to the antenna. In order to test the antenna along both the length and width direction, two SMA connector configurations are designed to feed the antenna along these two directions. In this chapter the experimental setup, procedure, results, and the comparison of the experimental results with the simulation are discussed.

5.1 Integrity testing of patch antenna under strain

In order to evaluate the maximum strain the copper film can sustain, the patch antennas were tested under tension using a compact mechanical tester. The compact mechanical tester, as shown in Figure 5.1, consists of a two translation stages; one of them is translated by a lead screw with fine threads and the other is connected to a load cell. The two ends of the Kapton strip coated with a metallic patch are mechanically clamped onto the two stages. Tensile load is applied to the Kapton strip by traversing the translational stage using the lead screw. The applied load is measured by the load cell. The analog voltage output of the load cell is acquired into a computer using a data acquisition card. For each loading, the corresponding strain value is calculated. A CCD camera assembled with a microscopic objective of 10X magnification is used for monitoring the metal integrity of the metallic patch under different strains. Figure 5.2

(a) shows the surface of the copper film under zero strain. Figure 5.2 (b) shows that the copper film under 3.5% strains. At this strain level, the metallic patch remained its structure integrity. Figure 5.2 (c) shows the copper peeling out of the Kapton surface at 5% strain.

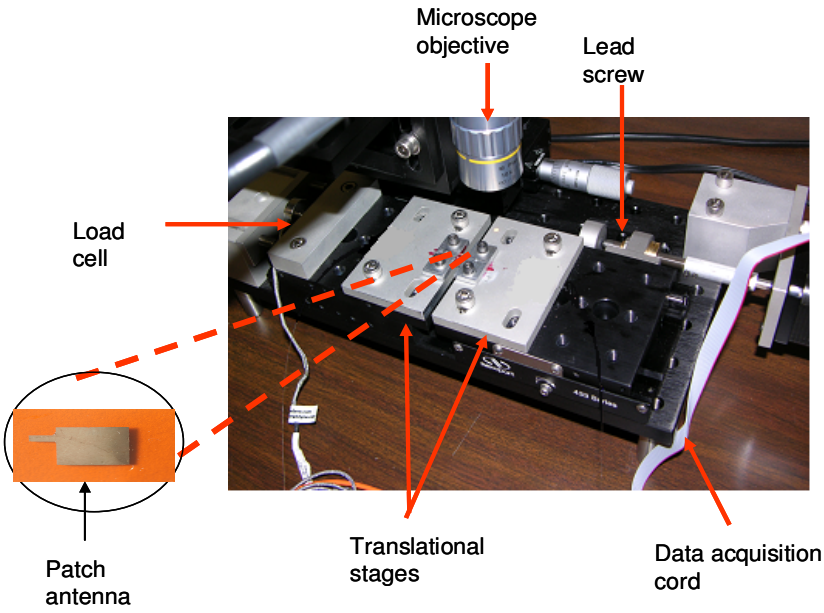

Figure 5.1: Micro tester setup

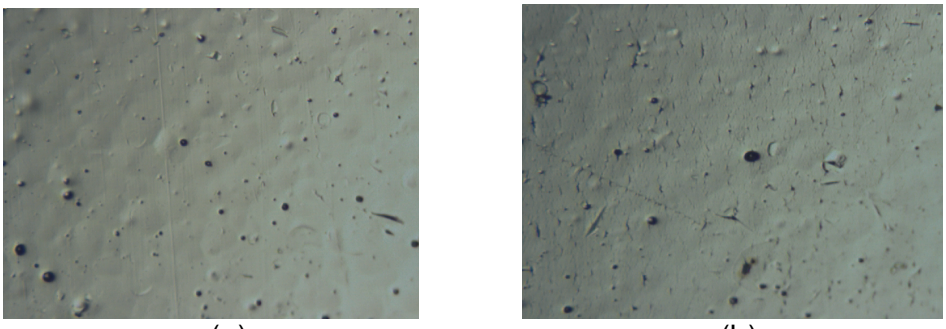

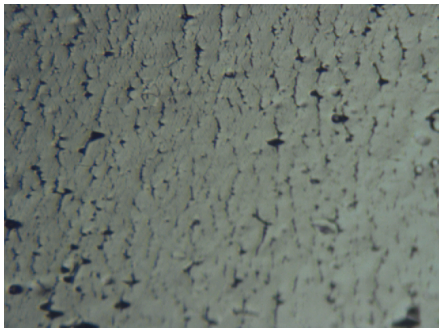

Figure 5.2: (a) Metal surface at 0% strain, (b) metal surface at 3.5 % strain and (c) metal surface at 5% strain

5.2 Design of a cantilever for strain measurement

5.2.1 Cantilever theory

A cantilever beam is a long slender structure that is fix-supported at only one end of the beam. Figure 5.3 shows a cantilever beam instrumented with a patch antenna and its cross section. The antenna is mounted at a distance from the fixed end of the cantilever beam. A load P is applied at the free end of the cantilever beam. Assume the length of the cantilever beam is L, the load P will generate a moment M at the location of the antenna. This moment can be calculated as [13]

$$M = -P(L - x)\,. \tag{5.1}$$

Based on the elastic flexure formula, the stress σ experienced by the patch antenna can therefore be calculated as

$$\sigma = \frac{-My}{I}\ , \tag{5.2}$$

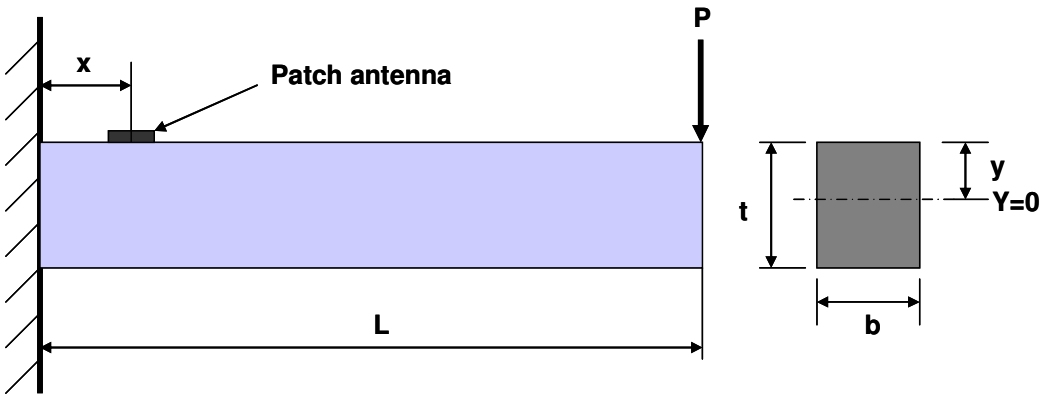

Figure 5.3: Cross sectional view of the cantilever.

where y is the distance measured from the neutral axis of the cantilever to the surface where the antenna is mounted. For a rectangular beam with a thickness t, y can be expressed as

$$y = \frac{t}{2}\ . \tag{5.3}$$

The moment of inertia I of the cantilever beam is expressed as

$$I = \frac{1}{12}bt^3, \tag{5.4}$$

where b is the base of the cantilver beam. Combining the Equations (5.1) and (5.2), the stress σ can be expressed as

$$\sigma = \frac{\left(-P(L-x)\right)\frac{t}{2}}{\frac{1}{12}bt^3} = \frac{6P(L-x)}{bt^3} \quad . \tag{5.5}$$

Based on Hooks Law, the stress σ is directly proportional to the strain ε_x by a constant called elastic modulus E, i.e.

$$\sigma = E\varepsilon_x \quad . \tag{5.6}$$

Combining Equations (5.5) and (5.6), the stain ε_x experienced by the patch antenna can be calculated as

$$\varepsilon_x = \frac{6P(L-x)}{Ebt^3} \quad . \tag{5.7}$$

5.2.2 Determination of cantilever dimensions

The cantilever is designed in such away that the patch antenna experiences 1% strain at a load of 50 pounds. In order to have a highly conductive material as the ground plane material for the patch antenna, Aluminum is chosen to be the cantilever material. At a distance of 0.25 inches from the free end of the cantilever beam, each side of the cantilever beam is machined with a circular slot to hold the weights properly. In order to mount a SMA connector on the edge of the cantilever, two mounting holes are drilled at the side wall of the cantilever beam. The mechanical drawing of the cantilever beam is shown in Figure 5.4. All the dimensions in the figure are in inches.

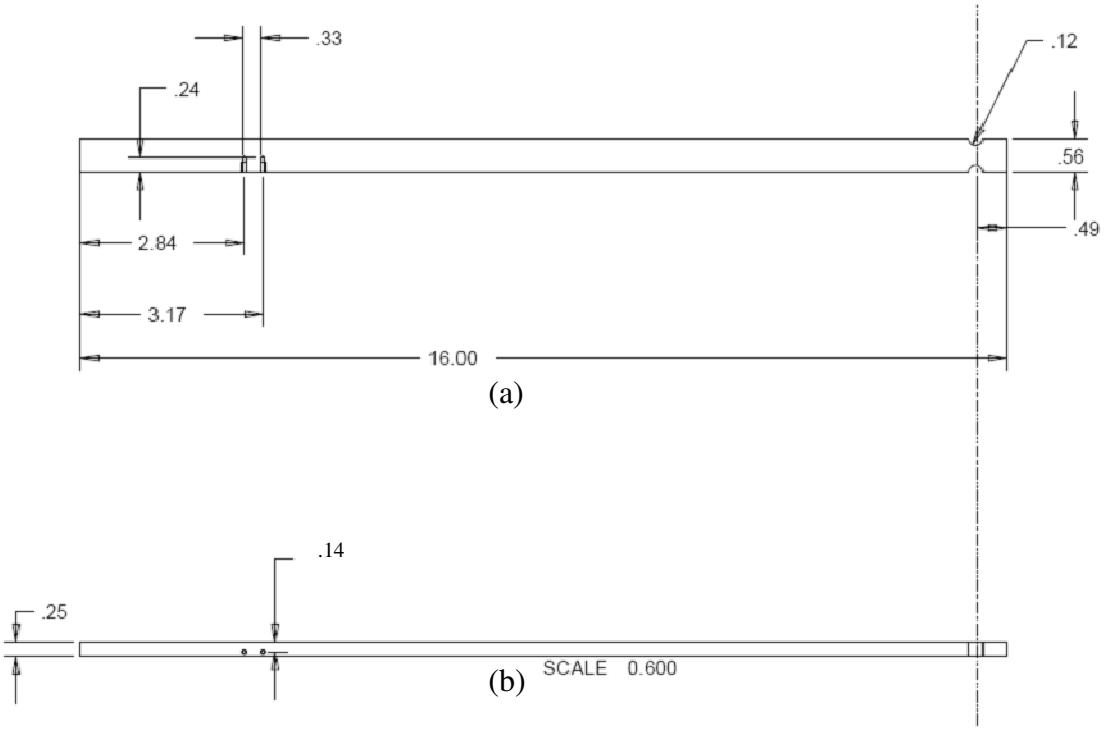

Figure 5.4: (a) Cantilever design top view (b) Side view

5.3 Antenna feeding configurations

The dual frequency patch antenna is bonded to the specimen using a conventional strain In order to evaluate the effect of strain along both the length and width direction on the antenna frequency, the patch antenna has to be stretched along these two directions. Therefore, two different SMA connector configurations are required.

5.3.1 SMA connector configurations

To test the antenna along the width direction, the patch can be bonded on the cantilever beam with its width direction parallel to the length direction of the cantilever beam, as

shown in Figure 5.5. A solder ball is placed at the end of SMA connector to ensure a sound electrical connection between the SMA tip and the antenna feeding line. In order to test the patch antenna along its length direction, the only feasible way to feed the patch antenna is to vertically hold the SMA connector and press the tip of the SMA connector onto the end of the antenna feeding line. A rectangular block is designed to hold the SMA connector at its flange so that the tip of the SMA connector rests firmly onto the patch antenna feed, as shown in Figure 5.6. The SMA connector is not directly soldered to the feed of the patch antenna because the bending of the cantilever beam puts immense pressure on the solder contact during mechanical testing. In order to prevent peeling the antenna copper film from the Kapton surface, the tip of the SMA connector is allowed to slide but remains a good connection to the antenna feeding line during the testing

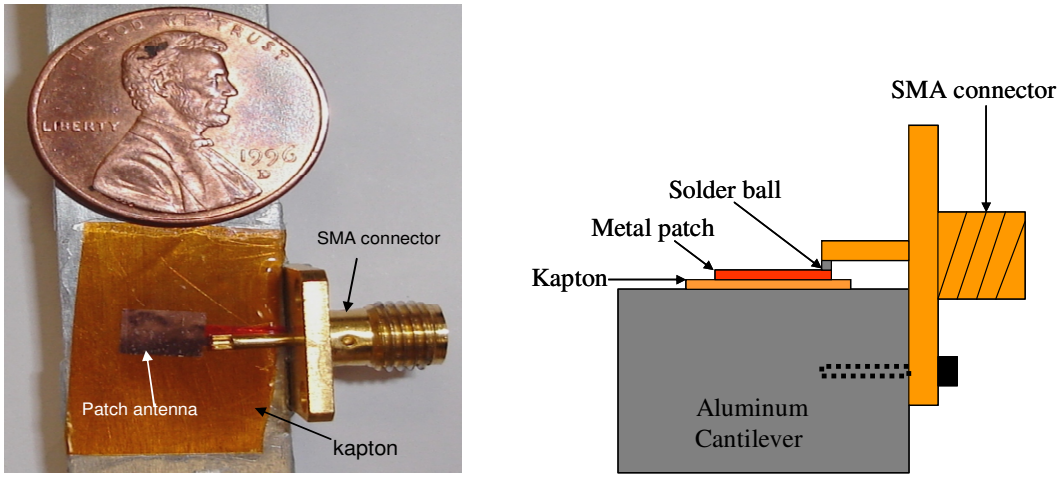

Figure 5.5: The SMA connector configuration for the width direction elongation of patch antenna.

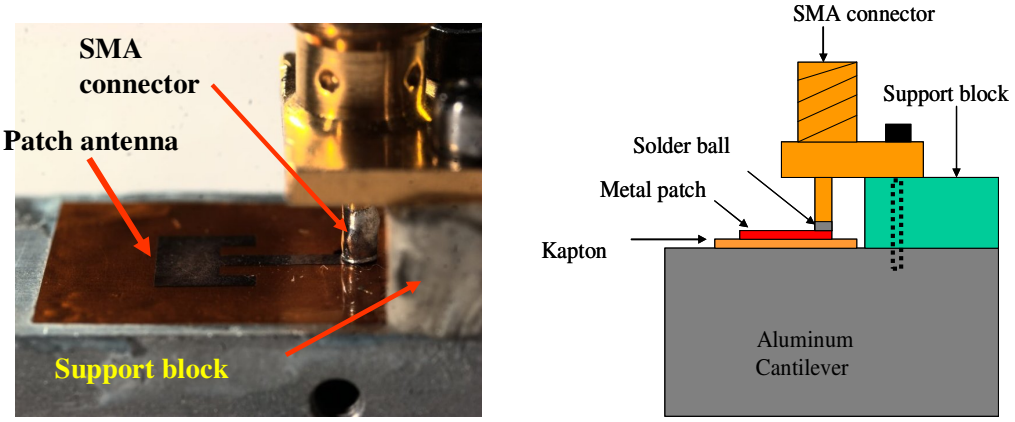

Figure 5.6: The SMA connector configuration for length direction elongation of patch antenna

5.4 Antenna characterization

The measured dual frequency of the antenna with the SMA connector is shown in Figure 5.7. The frequency corresponding to the width direction appears at 20.5 GHz and the frequency associated with the length direction appears at 17.2 GHz. These frequencies match well with the simulated frequency, which is 19.5 GHz for the width direction and 15 GHz in the length direction. The measured frequency response of a single frequency patch antenna is shown in Figure 5.8. The single frequency antenna has a measured frequency and a simulated frequency at 20.5 GHz and 19.5 GHz respectively. The slight mismatch of the measured and simulated frequency is due to the solder ball capacitance and the extra dielectric added due to the thin adhesive film between the patch antenna and the substrate.

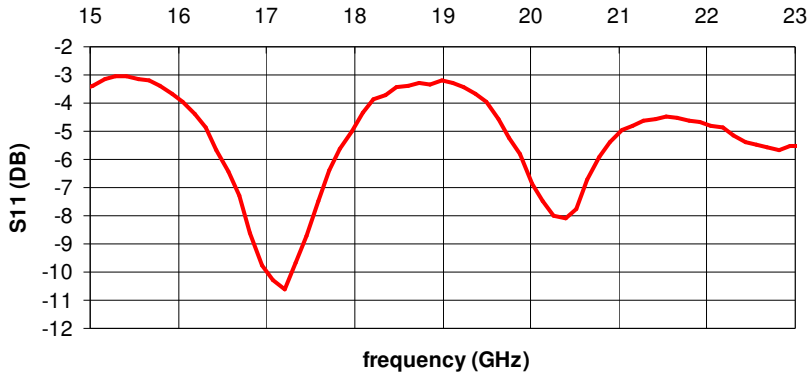

Figure 5.7: Measured dual frequency from the patch antenna.

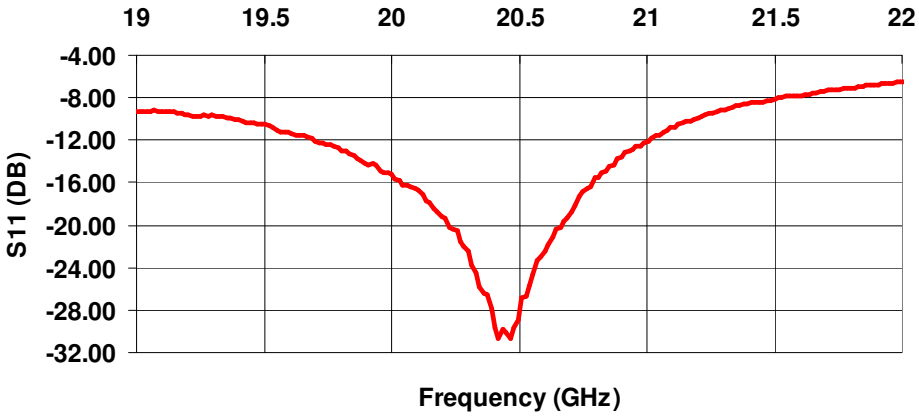

Figure 5.8: Measured single frequency from the patch antenna.

5.5 Experimental setup

The experimental set-up for the mechanical testing of the antenna patch is shown in Figure 5.9. One end of the cantilever is clamped to a workbench. The patch antenna is loaded in an increment of 5 lb (which corresponds to 0.1 % strain increase) until the total load reaches 35 lb. The load is limited to 35 lb in order to prevent yielding in the cantilever. The SMA connector of the patch antenna is connected to the network

analyzer. S_{11} parameter was measured to determine the frequency response of the patch antenna.

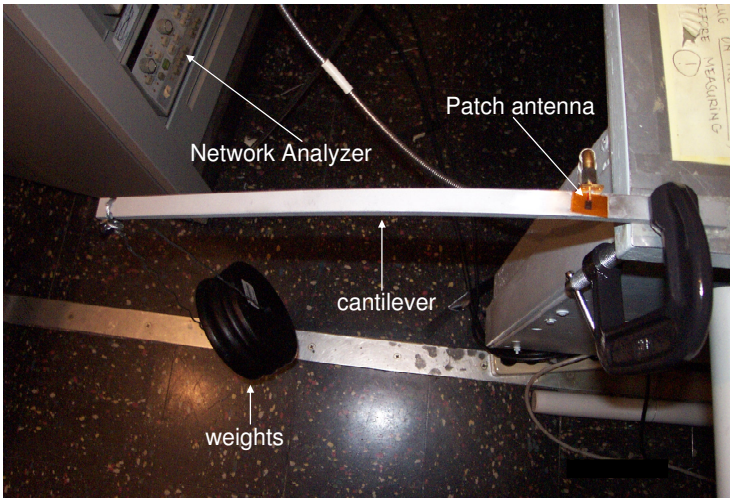

Figure 5.9: Experimental setup for mechanical testing of the patch antenna.

5.6 Experiment Results

The antenna frequency that corresponds to the width direction is 20.5 GHz. When the antenna is tested along the width direction, the Network Analyzer is set to acquire 400 data points from 19 GHz to 21GHz. Loads are applied to the cantilever beam up to 35 lb at an increment of 5 lb, which corresponds to 0% – 0.7% strain in steps of 0.1 % strain. The experimental results shown in Figure 5.10 clearly demonstrate the parallel shifts of the antenna frequency response as the applied load increases. This shift is consistent with the simulation results.

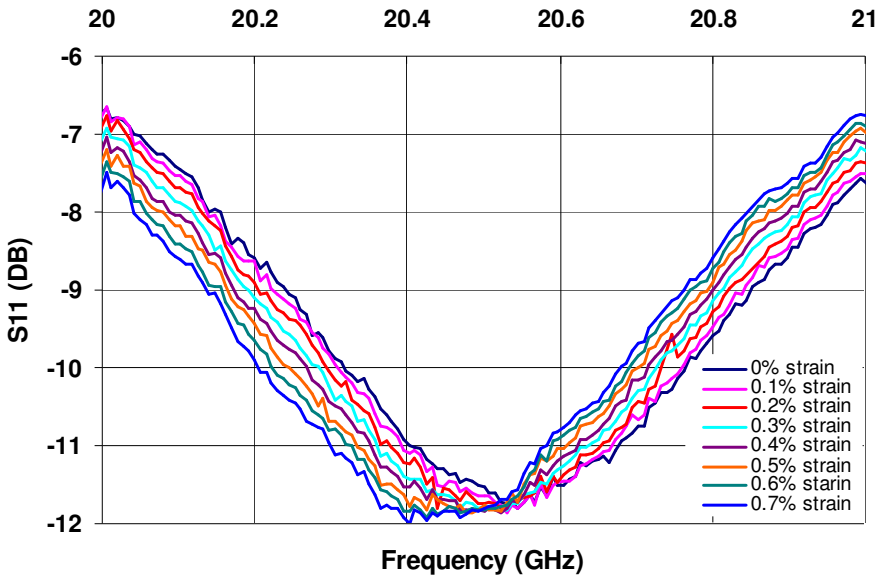

Figure 5.10: Frequency response of the antenna under strain in the width direction.

Similar procedure is followed to strain the antenna along the length direction. The loads are restricted to 30 lb (0.6%); further loading will cause the SMA connector to move away from the antenna feed, resulting in breaking the electrical contact between the SMA connector and the antenna patch. The sensitive frequency for the length direction elongation is 17.2 GHz. This frequency consistently shifts to the lower frequencies when the increases as shown in Figure 5.11.

Based on the above experimental results, it is evident that the dual frequency antenna is sensitive to strains along both the length and width directions. In case of a single frequency antenna, there is only one single current component flowing parallel to the length direction (TM_{010} mode) but there is no current flowing along the width direction (TM_{001} mode). Therefore, the single frequency antenna is insensitive to the width direction elongation. In order to validate this hypothesis, the single frequency antenna is bounded to the cantilever in such a way that the strain can be applied along the width

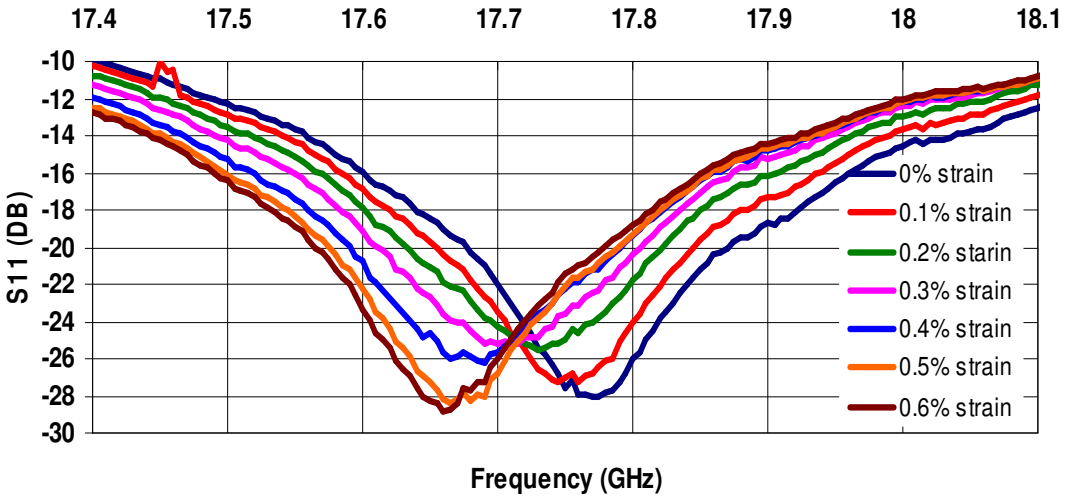

Figure 5.11: Measured frequency response of the antenna under strain in the length direction.

direction. Similar loading procedure is followed as of the loading of the dual frequency antenna. Figure 5.12 shows that there is no change in the resonant frequency of the antenna when the applied strains are along the width direction of the antenna.

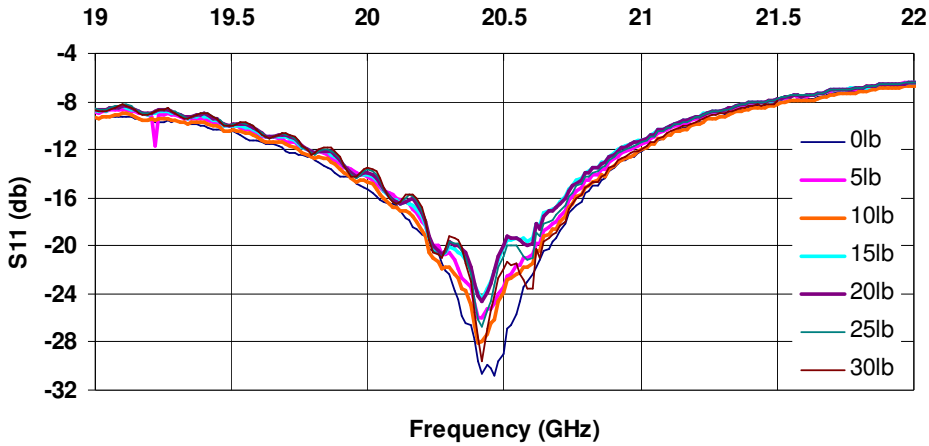

Figure 5.12: Frequency response of the antenna under strain along the width direction for single frequency antenna.

5.6.1 Data processing

Because the return loss of S11 at the antenna resonance frequency is very low, it is difficult to pin point the resonant frequency for each strain condition precisely. In order to overcome this problem, the shift of the resonant frequencies is calculated from the shift of the S11 curves at a set of 20 return loss values in the range of -9 db to -10db (width direction elongation) and -18 db to -20 db (length direction elongation). For each specific return loss value, the corresponding frequency of the S11 curve at each strain level is determined. In case there is no sampling point at a particular return loss, the corresponding frequency is calculated based on linear interpolation. The frequency shift for each strain level is calculated by taking the average of the frequency shifts at the 20 return loss values. The relative change in frequency is calculated by dividing the frequency shifts by the resonant frequency of the antenna when it is subjected to strain.

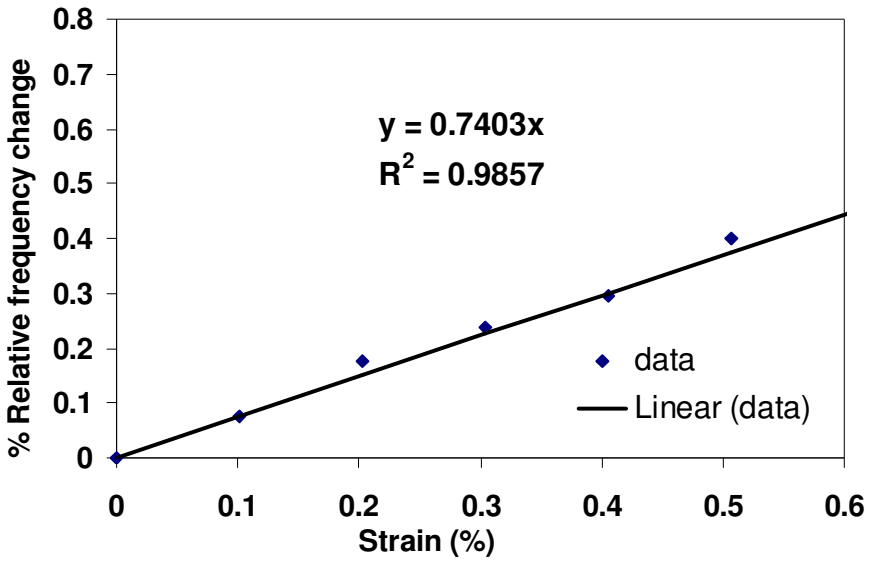

Figure 5.13: Experimental relationship between the percentage of change in antenna frequency and the applied strain along the width direction of a dual frequency patch antenna

Figure 5.13 shows the linear fitting of the percentage of change in frequency and the applied strains for the dual frequency patch antenna subjected to width direction elongation. The slope of the linear fitting represents the strain sensitivity of the sensor, which is 0.7403, corresponds to 15.2 kHz/microstrain. Similarly the relative change in frequency vs. strain for length direction elongation of the dual frequency antenna is shown in Figure 5.14. The strain sensitivity is found to be 0.899, which corresponds to 15.5 kHz/microstrain.

5.6.2 Comparison of experimental and simulation results

In chapter 3 the simulation results show that the strain sensitivity of the dual frequency patch antenna strain sensor along the width direction is 0.9725 while the measured strain sensitivity is 0.7403. Similarly, the strain sensitivity along the length direction is 0.983 from the simulation and 0.866 from the experiment. The measured strain

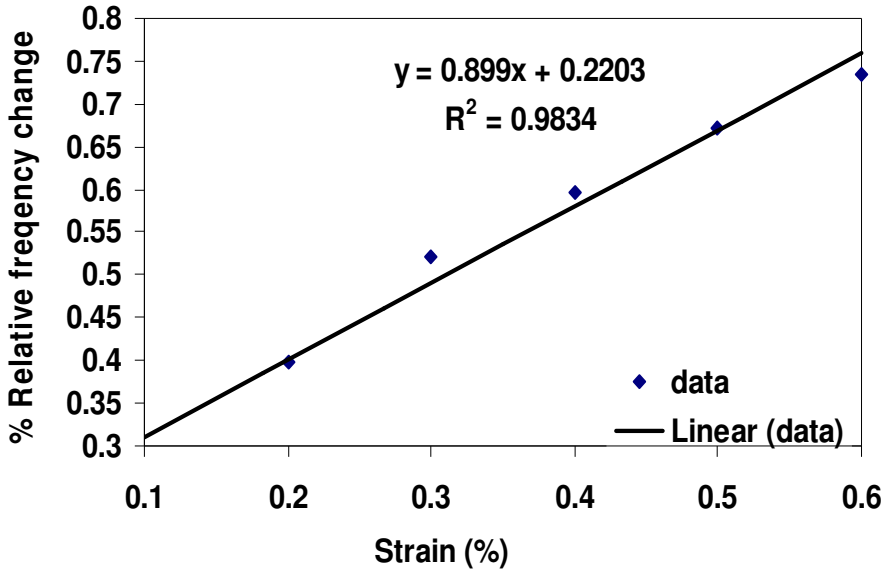

Figure 5.14: Experimental relationship between the percentage of change in antenna frequency and the applied strain along the Length direction of a dual frequency patch antenna

sensitivities are in good agreement with the simulation results. The slight mismatch of experimental results with simulated results may be contributed by the bonding between the Kapton substrate and the aluminum specimen. This may cause reduced strain transfer from the specimen to the metallic patch. Therefore, the patch antenna may experience less strain than expected.

Table 5.1: Comparison of simulation and experimental results.

Position	Simulation sensitivity (K)	Experimental sensitivity (K)
Length direction dual frequency	0.9830	0.8990
Width direction dual frequency	0.9725	0.7403
Width direction single frequency	0	0

CHAPTER 6

CONCLUSION

An innovative technique of measuring strain using a patch antenna is investigated. Patch antennas with dual and single frequency are designed based on the transmission line model. The design of the antennas was verified using an commercial EM simulation tool. The effects of strain along the length and width directions of the antennas on the antenna resonant frequency were simulated. The relative frequency change under different strain values is calculated and the strains vs. relative frequency change characteristics are plotted. The simulated strain sensitivities for length and width direction elongation of the dual frequency antenna are found to be 0.983 and 0.9725 respectively. For a single frequency antenna, the antenna resonant frequency is not sensitive to strains applied along the width direction. Both dual and single frequency patch antenna are fabricated on a 50 μm thick Kapton substrate, using a series of micromachining process such as photolithography, photoresist developing, deposition of copper, and liftoff process. A cantilever beam is designed for mechanical testing of the patch antenna. The patch antenna is bonded to the cantilever and is strained by applying weights at the end of the cantilever beam. Two antenna feeding configurations are devised to strain the antenna along both the length and width direction. The relative antenna frequency shift under each straining condition is calculated and the strain

sensitivity of the patch antenna are calculated from the experimental data. The measured strain sensitivities along the length and width directions are 0.740 and 0.899 respectively. The experimental results are in good agreement with the simulation results.

CHAPTER 7

FUTURE WORK

7.1 Introduction

In the future, the radiation parameters of a patch antenna can be measured via a non-contact reader, based on the principle of backscattering, as shown in Figure 7.1. The antenna reader serves as both the transmitter and the receiver. As a transmitter, the reader sends an incident EM wave toward the patch antenna. Upon intercepted by the patch antenna, the incident EM wave is scattered back by the patch antenna if the frequency of the incident wave matches the resonant frequency of the patch antenna. The backscattered EM wave is again received by the reader. The spectrum analysis of the received EM wave will determine the antenna radiation parameters (resonant frequency, return loss, etc.).

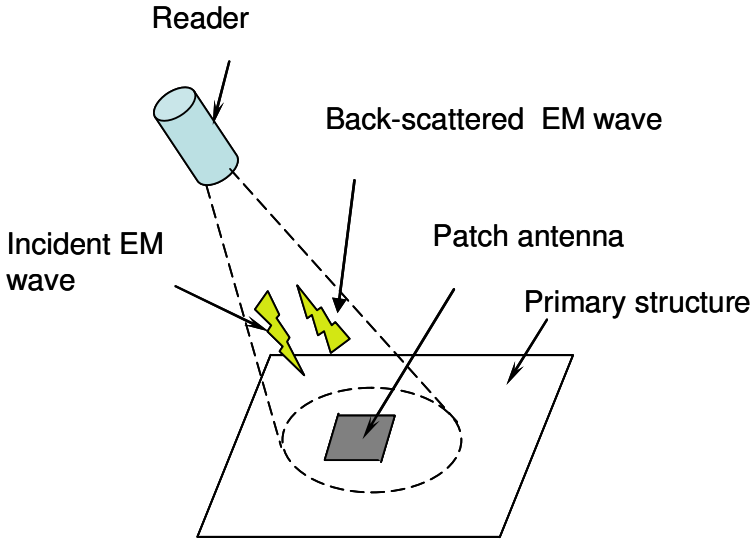

Figure 7.1: Non contact way of measuring resonant frequency of patch using a reader

Since the sensor doesn't require any external power, it provides a passive wireless technique of monitoring the strain.

7.2 Measurement configurations

The experimental configuration to measure the resonant frequency of the antenna in a noncontact way depends on the selection of the reader. The reader in this case can be a waveguide or horn antenna.

7.2.1 Waveguide as transmitter and receiver

In this measurement configuration, the waveguide is used as a both transmitter and receiver. The waveguide is connected to one port of the network analyzer. It is mounted on a three-axis translation stage for proper alignment between its opening and the patch antenna below it. Figure 7.2 shows the measurement configuration using a waveguide. The broadband EM signal from the Waveguide is incident on the patch antenna. For an open-circuited patch antenna, the backscattered EM signal consists of a structural scattering term and an antenna mode scattering term [8]. While the structural scattering term is independent of the antenna radiation characteristics, the antenna mode scattering term is solely governed by the antenna EM cavity. Gating the time domain antenna mode S11 signal and converting the signal back into the frequency domain gives the patch antenna resonant frequency. Figure 7.3 (a) shows a typical antenna mode time domain signal (b) shows the antenna resonant frequency.

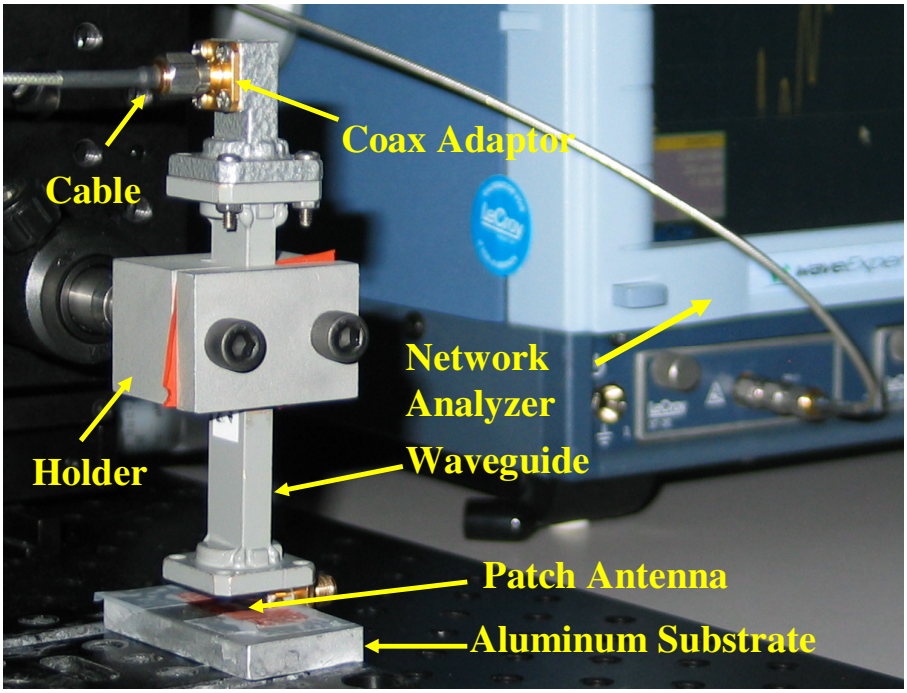

Figure 7.2: Experimental setup to measure resonant frequency of patch using a waveguide

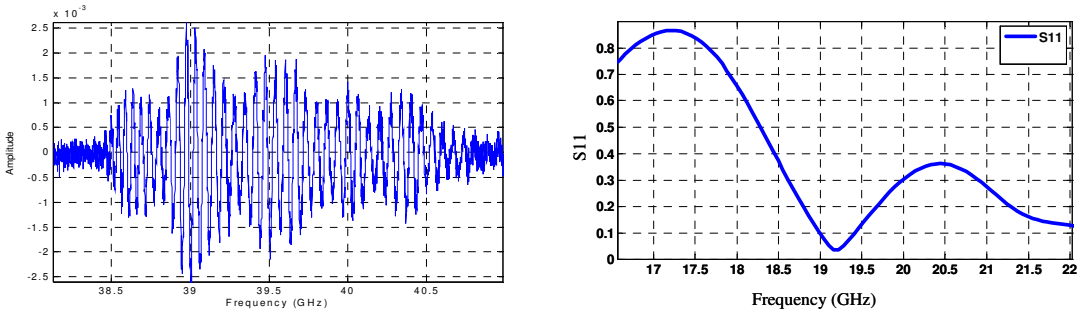

(a) (b)

Figure 7.3: (a) Gated time domain signal and (b) resonant frequency of patch antenna

7.2.2 Dual horn configuration

Figure 7.4 shows the antenna measurement configuration using two horn antennas. One of them is the transmitting antenna and the other is the receiving antenna. These two horn antennas are aligned towards the patch antenna whose frequency is to be measured. The transmitting horn antenna is connected to port1 and the receiving horn is

connected to port2 of the network analyzer. The broadband EM wave from the transmitter horn is impinged onto the patch antenna. The antenna mode reflected from the patch antenna is received by the receiving horn. The structural scattering mode can be prevented by aligning the two horns at an angle of 45^0 with respect to the surface of the patch antenna. The resonant frequency of patch antenna can be measured by monitoring the S_{12} or the S_{21} parameters..

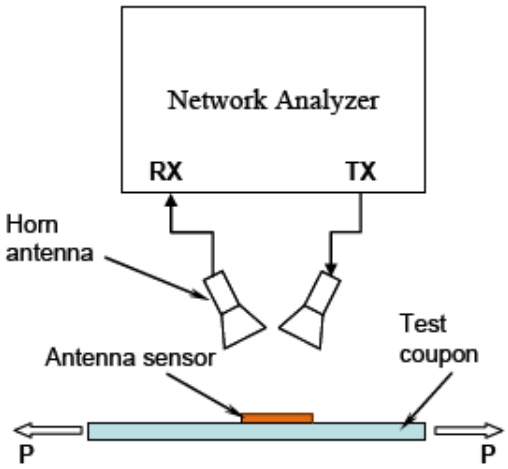

Figure: 7.4 Noncontact measurement of patch antenna's resonant frequency using two horn configuration.

In order to make sure that the two horn antennas are properly aligned with the patch antenna, a two port measurement between the transmitting horn and the patch antenna and between the receiving horn and the patch antenna should be carried out.

7.3 Discussion

The challenge facing in using the waveguide as the transmitting and receiving antenna is that the waveguide is highly sensitive to its position. A small movement in the waveguide position will disturb its alignment with the patch. In addition, the waveguide

needs to be placed very close to the patch since it has a low gain and directivity. The horn antenna has a high gain and directivity. Since the horn antenna has a large beam size, the measurements are not very sensitive to the horn's position with respect to patch antenna. However, the horn antenna usually has a large far-field distance, typically 2.5 meters at high frequencies, and it has to be operated in the far field to get reliable measurements. In case of two horn configurations, the RF power of 10 mW from the network analyzer is sent through the horn. This power attenuates when it reaches the patch antenna located at the horn's far field distance. In order to determine the patch antenna's resonant frequency, the backscattered signal from the patch antenna has to reach the receiving horn. There is a huge power loss in the entire process. As a result, we may not be able to measure the resonant frequency from the patch due to low signal to noise ratio. The problem can be solved using an amplifier in the path between the transmitter and the network analyzer.

APPENDIX A

MATERIAL DATA SHEETS

A.1 PHOTORESIST DATASHEET

SHIPLEY

MICROPOSIT® S1800® SERIES PHOTO RESISTS

MICROPOSIT S1800 SERIES PHOTO RESISTS are positive photoresist systems engineered to satisfy the microelectronics industry's requirements for advanced IC device fabrication. The system has been engineered using a toxicologically safer alternative casting solvent to the ethylene glycol derived ether acetates. The dyed photoresist versions are recommended to minimize notching and maintain linewidth control when processing on highly reflective substrates.

MICROPOSIT S1800 SERIES PHOTO RESISTS FEATURE:

Product Assurance
- Lot-to-lot consistency through state-of-the-art physical, chemical and functional testing
- Filtered to 0.2 µm absolute

Coating Properties
- [1]Cellosolve® Acetate and xylene free
- Striation-free coatings
- Excellent adhesion
- Excellent coating uniformity
- A variety of standard viscosities are available for single-layer processing

Exposure Properties
- Optimized for G-Line exposure
- Effective for broad-band exposure
- Reflective notch and linewidth control using dyed versions

Develop Properties
- Optimized for use with the MICROPOSIT® MF®-319 Metal-Ion-Free DEVELOPER family
- Compatible with Metal-Ion-Bearing MICROPOSIT DEVELOPERS

Removal Property
- Residue-free photoresist removal using standard MICROPOSIT REMOVERS

High Resolution Process Parameters (Refer to Figure 1)	
Substrate:	Polysilicon
Photoresist:	MICROPOSIT®S1813® PHOTO RESIST
Coat:	12,300Å
Softbake:	115°C/60 sec. Hotplate
Exposure:	Nikon 1505 G6E, G-Line (0.54 NA), 150 mJ/cm^2
Develop:	MICROPOSIT® MF®-321 DEVELOPER
	15 + 50 sec. Double Spray Puddle (DSP) @ 21°C

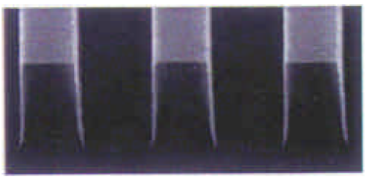

0.80 µm Lines/Spaces

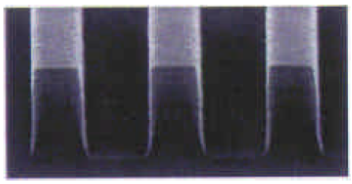

0.70 µm Lines/Spaces

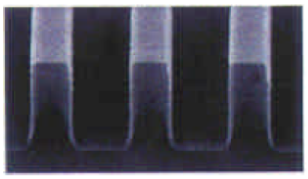

0.60 µm Lines/Spaces

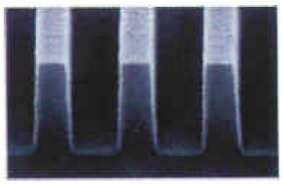

0.50 µm Lines/Spaces

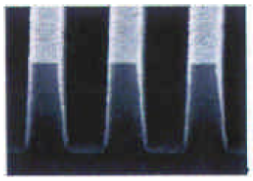

0.48 µm Lines/Spaces

Masking Linearity SEMS
Figure 1.

Instructions for Use

The following instructions cover the use of MICROPOSIT S1800 SERIES PHOTO RESISTS for all levels of microelectronic device fabrication. Exact process parameters are application and equipment dependent.

Substrate Preparation

MICROPOSIT S1800 SERIES PHOTO RESISTS work well with the hexamethyldisilazane based MICROPOSIT PRIMERS. Concentrated MICROPOSIT PRIMER is recommended when vacuum vapor priming. Diluted PRIMER is recommended for liquid phase priming applications.

Coat

MICROPOSIT S1800 SERIES PHOTO RESISTS provide uniform defect-free coatings over a wide range of film thicknesses. The film thickness versus spin speed plots displayed in **Figures 1 and 2** provide the information required to properly select a MICROPOSIT S1800 PHOTO RESIST version to meet process dependent thickness specifications. Maximum coating uniformity is typically attained between the spin speeds of 3500 rpm and 5500 rpm.

Process Parameters (Refer to Figures 1 and 2)	
Substrate	Silicon
Coat	SVG 81
Softbake	115°C/60 seconds Hotplate
Measure	Nanometrics 210

The dispersion curve and Cauchy equation displayed in **Figure 3** describe how the refractive index of the photoresist film varies as a function of the wavelength of light incident upon the film. This information is required to program ellipsometric and other optically based photoresist measuring equipment.

Process Parameters (Refer to Figure 3)	
Substrate	Silicon
Coat	13,675Å
Softbake	115°C/60 seconds Hotplate
Measure	Prometrix SM300

MICROPOSIT S1800 PHOTO RESIST UNDYED SERIES

Figure 1. Spin Speed Curves

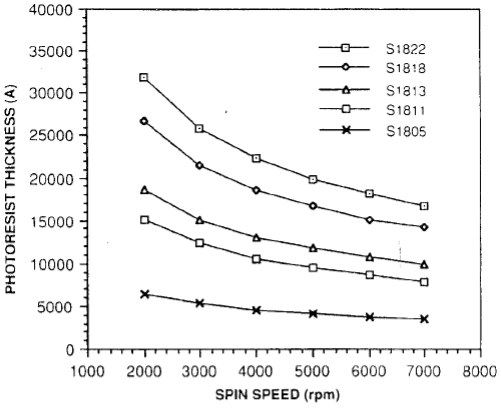

MICROPOSIT S1800 PHOTO RESIST DYED SERIES

Figure 2. Spin Speed Curves

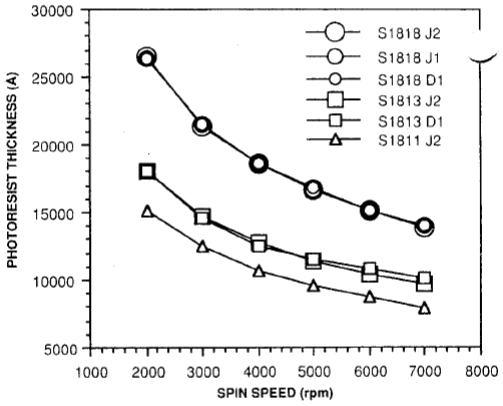

MICROPOSIT® S1813® PHOTO RESIST

Figure 3. Dispersion Curve

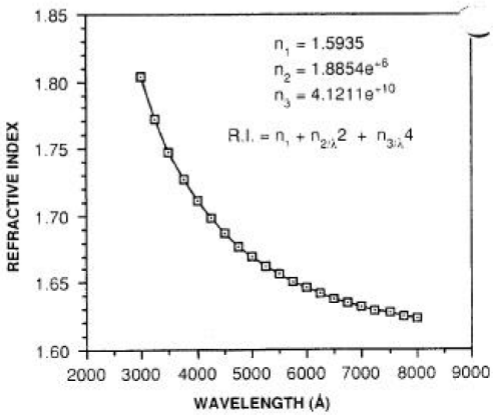

Exposure

Proper film thickness selection is critical in order to reduce photospeed and critical dimension variability. The interference curves displayed in **Figure 4** illustrate the photospeed variability as a function of film thickness. Dyed versions suppress the interference effects which are more pronounced when exposing with monochromatic light sources and when using reflective substrates.

Process Parameters (Refer to Figure 4)	
Substrate	Silicon
Coat	GCA 1006 ^{2}WAFERTRAC®
Softbake	115°C/60 seconds Hotplate
Expose	GCA 8500 G-Line (0.35 NA)
Developer	MF-321 /10 + 30 DSP @ 21°C

MICROPOSIT S1800 SERIES PHOTO RESISTS can be exposed with light sources in the spectral output range of 350 nm -450 nm. The exposure properties have been optimized for use at 436 nm. **Figures 5 and 6** show the absorbance spectrums for MICROPOSIT S1813 and S1813 J2® PHOTO RESISTS.

Process Parameters (Refer to Figures 5 and 6)	
Substrate	Quartz
Coat	12,300Å
Softbake	115°C/60 seconds Hotplate
Expose	Oriel Scanning Wedge
Measure	Hewlett Packard 8450A Spectrophotometer

Table 1 summarizes the Dill parameters for each MICROPOSIT S1800 SERIES PHOTO RESIST version. Dill parameters are used in optical exposure models such as SAMPLE and PROLITH.

MICROPOSIT S1800 SERIES PHOTO RESISTS
Table 1. Dill Parameters

	365 nm		436 nm	
Photoresist	A (μm^{-1})	B (μm^{-1})	A (μm^{-1})	B (μm^{-1})
S1813	1.07	0.31	0.61	0.08
S1813 D1	1.05	0.34	0.58	0.26
S1811 J2	1.07	0.49	0.59	0.61
S1818 J1	1.06	0.42	0.57	0.37

MICROPOSIT S1813 and S1813 J2 PHOTO RESIS
Figure 4. Interference Curves

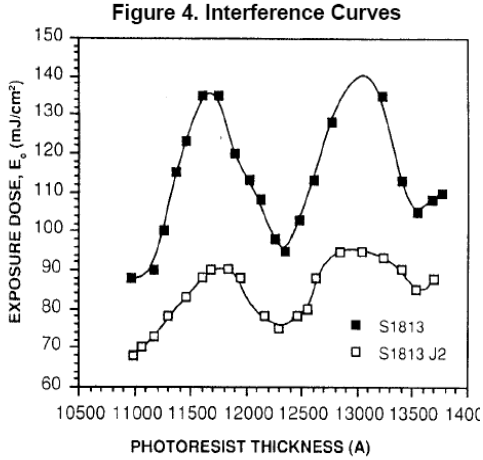

MICROPOSIT S1813 PHOTO RESIST
Figure 5. Absorbance Spectrum

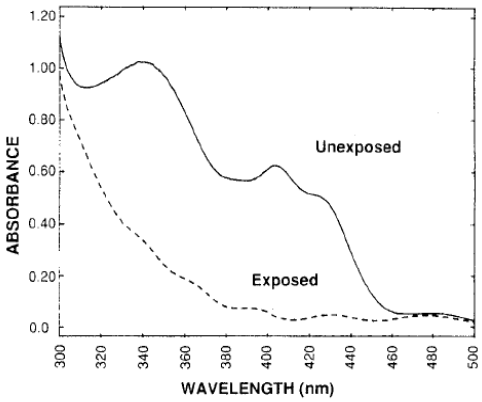

MICROPOSIT S1813 J2 PHOTO RESIST
Figure 6. Absorbance Spectrum

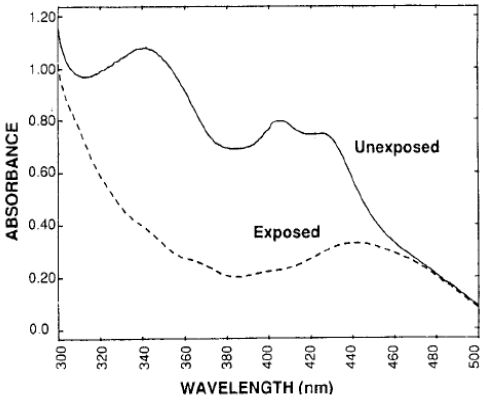

Figure 7 displays a contrast curve for MICROPOSIT S1813 PHOTO RESIST developed with MICROPOSIT® MF®-321 DEVELOPER. In general, high contrast values correlate to higher angle wall profiles.

Process Parameters (Refer to Figure 7)	
Substrate	Silicon
Coat	12,300Å
Softbake	115°C/60 seconds Hotplate
Expose	GCA 8500 G-Line (0.35 NA)
Develop	MF-321 /10 + 30 DSP @ 21°C

DEVELOP

MICROPOSIT S1800 SERIES PHOTO RESISTS are compatible with both Metal-Ion-Free (MIF) and Metal-Ion-Bearing (MIB) developers. A photoresist and developer system is dependent upon specific application requirements. Contact your local Shipley Technical Sales Representative for additional product information.

Figures 8 thru 10 illustrate the lithographic functionality of MICROPOSIT S1813 PHOTO RESIST using process parameters designed to maximize resolution while maintaining excellent exposure and focus latitude (refer to SEM photographs in **Figure 1**). The functional lithographic responses are summarized in **Table 2**.

Process Parameters (Refer to Figures 8 thru 10)	
Substrate	Silicon
Coat	12,300Å
Softbake	115°C/60 seconds Hotplate
Expose	Nikon 1505 G6E G-Line (0.54 NA)
Develop	MF-321 /15 + 50 DSP @ 21°C

MICROPOSIT S1813 PHOTO RESIST with MICROPOSIT MF-321 DEVELOPER

Table 2. Functional Lithographic Summary Data

Sizing Energy	150 mJ/cm^2 (1.3 E_0)	
Resolution	0.48 µm	
Masking Linearity (±10% CD)	0.50 µm	
	1.0µm L/S	0.60 µm L/S
Exposure Latitude (±10% CD)	65%	45%
Focus Latitude (±10% CD) ≥ 85° Wall Angle	2.25 µm	1.25 µm

MICROPOSIT S1813 PHOTO RESIST

Figure 7. Contrast Curve

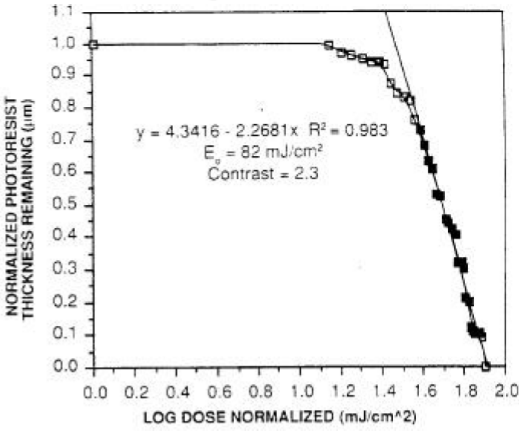

MICROPOSIT S1813 PHOTO RESIST

Figure 8. Masking Linearity Plot

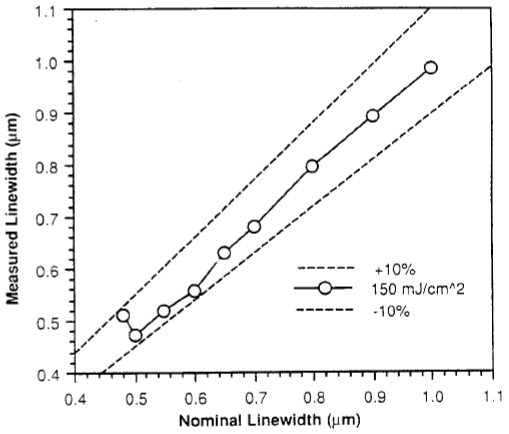

MICROPOSIT S1813 PHOTO RESIST

Figure 9. Exposure Latitude Plot

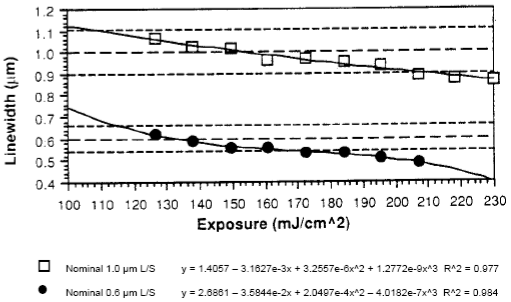

A.2 KAPTON DATASHEET

Table 1
Physical Properties of Kapton® HN at 23°C (73°F)

Property	Unit	1 mil 25µm	2 mil 50µm	3 mil 75µm	5 mil 125µm	Test Method
Ultimate Tensile Strength at 23°C, (73°F) at 200°C (392°F)	psi (MPa)	33,500(231) 20,000(139)	33,500(231) 20,000(139)	33,500(231) 20,000(139)	33,500(231) 20,000(139)	ASTM D-882-91, Method A*
Ultimate Elongation at 23°C, (73°F) at 200°C (392°F)	%	72 83	82 83	82 83	82 83	ASTM D-882-91, Method A
Tensile Modulus at 23°C, (73°F) at 200°C (392°F)	psi (GPa)	370,000 (2.5) 290,000 (2.0)	370,000 (2.5) 290,000 (2.0)	370,000 (2.5) 290,000 (2.0)	370,000 (2.5) 290,000 (2.0)	ASTM D-882-91, Method A
Density	g/cc	1.42	1.42	1.42	1.42	ASTM D-1505-90
MIT Folding Endurance	cycles	285,000	55,000	6000	5,000	ASTM D-2176-89
Tear Strength-propagating (Elmendorf), N (lbf)		0.07 (0.02)	0.21 (0.02)	0.38 (0.02)	0.58 (0.02)	ASTM D-1922-89
Tear Strength, Initial (Graves), N (lbf)		7.2 (1.6)	16.3 (1.6)	26.3 (1.6)	46.9 (1.6)	ASTM D-1004-90
Yield Point at 3% at 23°C, (73°F) at 200°C (392°F)	MPa (psi)	69 (10,000) 41 (6000)	69 (10,000) 41 (6000)	69 (10,000) 41 (6000)	69 (10,000) 41 (6000)	ASTM D-882-91
Stress to produce 5% elong. at 23°C, (73°F) at 200°C (392°F)	MPa (psi)	90 (13,000) 61 (9000)	90 (13,000) 61 (9000)	90 (13,000) 61 (9000)	90 (13,000) 61 (9000)	ASTM D-882-92
Impact Strength at 23°C, (73°F)	N•cm•(ft lb)	78 (0.58)	78 (0.58)	78 (0.58)	78 (0.58)	DuPont Pneumatic Impact Test
Coefficient of Friction, kinetic (film-to-film)		0.48	0.48	0.48	0.48	ASTM D-1894-90
Coefficient of Friction, static (film-to-film)		0.63	0.63	0.63	0.63	ASTM D-1894-90
Refractive Index (sodium D line)		1.70	1.70	1.70	1.70	ASTM D-542-90
Poisson's Ratio		0.34	0.34	0.34	0.34	Avg. three samples, Elongated at 5, 7, 10%
Low temperature flex life		pass	pass	pass	pass	IPC-TM-650, Method 2.6.18

Table 2
Thermal Properties of Kapton® HN Film

Thermal Property	Typical Value	Test Condition	Test Method
Melting Point	None	None	ASTM E-794-85 (1989)
Thermal Coefficient of Linear Expansion	20 ppm/°C (11 ppm/°F)	-14 to 38°C (7 to 100°F)	ASTM D-696-91
Coefficient of Thermal Conductivity, W/m•K $\frac{cal}{cm \bullet sec \bullet °C}$	0.12 2.87×10^{4}	296 K 23°C	ASTM F-433-77 (1987)
Specific Heat, J/g•K (cal/g•°C)	1.09 (0.261)		Differential calorimetry
Heat Sealability	not heat sealable		
Solder Float	pass		IPC-TM-650, method 2.4.13A
Smoke Generation	D_m=<1	NBS smoke chamber	NFPA-258
Shrinkage, % 30 min at 150°C 120 min at 400°C	 0.17 1.25		IPC-TM-650 Method 2.2.4A; ASTM D-5214-91
Limiting Oxygen Index, %	37-45		ASTM D-2863-87
Glass Transition Temperature (T_g)	A second order transition occurs in Kapton® between 360°C(680°F) and 410°C(770°F) and is assumed to be the glass transition temperature. Different measurement techniques produce different results within the above temperature range.		

Table 3
Typical Electrical Properties of Kapton® HN Film at 23°C (73°F), 50% RH

Property Film Gage	Typical Value		Test Condition	Test Method
Dielectric Strength	V/m kV/mm	(V/mil)	60 Hz 1/4 in electrodes 500 V/sec rise	ASTM D-149-91
25 µm (1 mil)	303	(7700)		
50 µm (2 mil)	240	(6100)		
75 µm (3 mil)	205	(5200)		
125 µm (5 mil)	154	(3900)		
Dielectric Constant			1 kHz	ASTM D-150-92
25 µm (1 mil)	3.4			
50 µm (2 mil)	3.4			
75 µm (3 mil)	3.5			
125 µm (5 mil)	3.5			
Dissipation Factor	Ω		1 kHz	ASTM D-150-92
25 µm (1 mil)	0.0018			
50 µm (2 mil)	0.0020			
75 µm (3 mil)	0.0020			
125 µm (5 mil)	0.0026			
Volume Resistivity	•cm			ASTM D-257-91
25 µm (1 mil)	1.5×10^{17}			
50 µm (2 mil)	1.5×10^{17}			
75 µm (3 mil)	1.4×10^{17}			
125 µm (5 mil)	1.0×10^{17}			

APPENDIX B

MATLAB PROGRAMS

B.1 PROGRAM TO CALCULATE ANTENNA DIMENSIONS UNDER STRAIN

```
% TO CALCULATE EFFECT OF STRAIN ON ANTENNA DIMENSIONS AND
RESONANT FREQUENCY
clear; clc;
w0=0.005056; % width of patch, in meter
L0=0.004037  % length of patch in meter
t0=50e-6;       % thickness of substrate, in meter
Epsilon=3.4;   % dielectric constant of the substrate

strain=[0:0.2:1]*1e-2;          % strain of antenna
mu_c=0.3;                       % poissons ratio of the conductor
mu_s=0.3;                       % poisson's ratio of the substrate
L=(1+strain)*L0;                % length of patch after strain
w=(1-mu_c*strain)*w0;           % width of patch after strain
t=(1-mu_s*strain)*t0;           % thickness of the substrate after strain

Rwt=w./t;

%alpha=1+1/49*log((Rwt^4+(1/52*Rwt)^2)/(Rwt^4+0.432))+1/18.7*log(1+(1/18.1*R
wt).^3);

Ereff=(Epsilon+1)/2+(Epsilon-1)/2*(1+10./Rwt).^(-0.5)  % effective dielectric
constants of substrate

dL=0.412*(Ereff+0.3).*(Rwt+0.264)./(Ereff-0.258)./(Rwt+0.813).*t  % line extension

fr=2.998e8/2./sqrt(Ereff)./(L+2*dL);  % resonant frequency of the antenna

plot(strain*100, fr/1e9); title('Frequency vs. strain');xlabel('strain (%)');ylabel('R.F
(GHz)'); grid on;

(max(fr)-min(fr))/(max(strain)*1e6)
```

B.2 INTERPOLATION OF UNKNOWN DATA POINTS

```
function Rxi=f_R_xi(x, R, xi)
% function Rxi=R_kxi(x, R_meas, xi)
% find the value R at xi if the relationship between x and R is given
% by R at location x. x and R are sort in ascend order
% Inputs:
%   x-sampled locations
%   R-value at sampled locations
%   xi-specified locations
% Outputs:
%   Rxi-value at xi derived from x, R
N=length(xi);

for ii=1:N
   index=find(x==xi(ii));

   if (length(index)==1)
      Rxi(ii)=R(index);
   else
      index=find(x<xi(ii));
      p_l=index(length(index));
      x_l=x(p_l);
      index=find(x>xi(ii));
      p_h=index(1);
      x_h=x(p_h);
      Rxi(ii)=R(p_l)+(xi(ii)-x_l)/(x_h-x_l)*(R(p_h)-R(p_l));
   end
end

[M,N]=size(R);

if N==1
   Rxi=Rxi.';
end
```

REFERENCES

[1] Karashima T et al. “Distributed Temperature sensing using stimulated Brillouin Scattering in Optical Silica Fibers”, Optics Letters, Vol. 15, pp. 1038 , (1990).

[2] Hong-Liang W, Xue-Guang Q, Hai-Wei F, De-Quan F, Dong-Ming L “FBG sensor of measuring pressure with lag of stress active compensation and with temperature active compensation” Journal of Optoelectronics Laser, Vol.19, No.1, pp.1-5,January, 2008.

[3] Thévenaz L et al. “Truly Distributed Strain and Temperature Sensing Using Embedded Optical Fibers”, Smart Structure and Materials Conference, San Diego USA, SPIE Vol. 3330, pp. 301-314, 1998.

[4] Yeo Y.L, Eckstein D, McKinley B, Boswell L.F, Sun T Grattan K.T.V, ” Demonstration of a fiber-optic sensing technique for the measurement of moisture absorption in concrete” Smart Materials and Structures, Vol 15, No. 2, pp N40-N45, April 1, 2006.

[5] Hong-Nan L, Dong-Sheng L, Gang-Bing S “Recent applications of fiber optic sensors to health monitoring in civil engineering” Engineering Structures, Vol 26, No. 11, pp. 1647-1657, September, 2004,

[6] Selvarajan A “MEMS and photonics technologies for structural health monitoring” Proceedings of SPIE -The International Society for Optical Engineering, Vol 5062, No.1, pp. 10-17, 2002

[7] Jerome L.P “Design of a wireless active sensing unit for localized structural health monitoring” Structural Control and Health Monitoring, Vol. 12, No. 3-4, pp. 405-423, July/December, 2005,

[8] Balanis C, “Antenna Theory: Analysis and Design”, John Wiley publications, Third Edition,2005

[9] Warren L.S, Gary A.T “Antenna theory and design”, John Wiley publications, Second Edition,1998

[10] Jin-Sen C, Kin-Long W, “A single-layer dual-frequency rectangular microstrip patch antenna using a single probe feed” Microwave and optics technology letters ,Vol. 11, No. 2, pp.83,February5, 1996

[11] Bhartia P, Rao K.V.S, Tomar R.S ” Millimeter-Wave Microstrip and Printed Circuit Antennas” Artech House inc., 1991

[12] Jaeger R.C “Introduction to Microelectronic fabrication” Prentice Hall, Second Edition, 2002

[13] Beer F.P and Johnston E.R, Jr., Mechanics of Materials, McGraw Hill, Third Edition, 2002.

BIOGRAPHICAL INFORMATION

Uday Tata received his Bachelors of Engineering in Instrumentation Engineering from Osmania University, Hyderabad, India in June 2006. He is pursuing his Master of Science in Electrical Engineering from the University of Texas at Arlington, U.S.A. His research interests include optical fiber and wireless sensors for structural health monitoring and MEMS based microsensors for biomedical applications. During his research work at the Advanced Sensor Technology Laboratory, he has published one journal and three conferences papers. He has two US patents and disclosures.